Elsevier Editorial System(tm) for Chemical Geology

Manuscript Draft

Manuscript Number: CHEMGE9903R1

Title: The 2013 eruption of Chaparrastique volcano (El Salvador): Effects of magma storage, mixing, and decompression

Article Type: Research paper

Keywords: Chaparrastique volcano; Central American volcanic arc; magma mixing; magma decompression

Corresponding Author: Professor. Silvio Mollo,

Corresponding Author's Institution: Sapienza - Università di Roma

First Author: Piergiorgio Scarlato

Order of Authors: Piergiorgio Scarlato; Silvio Mollo; Elisabetta Del Bello; Albrecht von Quadt; Richard J. Brown; Eduardo Gutierrez; Bettina Martinez-Hackert; Paolo Papale

Abstract: On December 29, 2013, an isolated vulcanian-type eruption occurred at Chaparrastique volcano (El Salvador) after 12 years of inactivity. The eruption was classified as VEI 2 and produced an ash plume with a maximum height of ~9 km. Textural and compositional data from phenocrysts from the erupted products have been integrated with geochemical and isotopic information from bulk rocks to elucidate the magmatic processes responsible for the reawakening of volcanic activity. Phenocrysts consist of Fo-rich poikilitic olivines hosting high-Mg titanomagnetites, and Fo-poor olivines coexisting with low-Mg titanomagnetites. Mineral-melt equilibria suggest an origin for the distinct phenocryst populations by mixing between a high-T (~1,130-1,150 °C), basaltic magma with fO2 (NNO buffer) typical of the lower crust in arc systems and a low-T (~1,060-1,080 °C), basaltic andesitic magma with fO2 (NNO+1 buffer) commonly encountered in shallower, more oxidized crustal reservoirs. Thermobarometry based on Fe-Mg exchange between orthopyroxene and clinopyroxene constrains the crystallization before eruption at relative low-P (~150-250 MPa) and low-T (~1,000-1,050 °C). Mixing between two chemically distinct magmas is also evidenced by the occurrence of reverse zoned plagioclase phenocrysts with resorbed sodic cores and re-growth of sieve-textured calcic mantles. Conversely, plagioclase rims exhibit disequilibrium compositions addressed to decompression kinetics (~10-3 MPa/s) driven by rapid magma ascent to the surface (~0.03 m/s).
Major and trace element modelling excludes fractional crystallization as the primary mechanism controlling the bulk rock variability, whereas geochemical data align along a mixing trend between two end-members representative of the primitive basalt and the differentiated basaltic andesite. Trace element and isotope data indicate that the primary source of magmatism is an enriched MORB-like mantle with the contribution of fluxes of metasomatic fluids and/or melts produced by the subducted slab. The role played by slab-fluid inputs of carbonate origin and slab-melts from the hemipelagic sediments seems to be minimal.
Assimilation/contamination processes of magmas by crustal rocks are also

negligible. In contrast, the geochemical signature of magmas is greatly influenced by slab-derived aqueous fluids produced prevalently by progressive dehydration of marine sediments and altered basaltic crust.

The 2013 eruption of Chaparrastique volcano (El Salvador): Effects of magma storage, mixing, and decompression

Piergiorgio Scarlato[1], Silvio Mollo[1,2], Elisabetta Del Bello[1], Albrecht von Quadt[3], Richard J. Brown[4], Eduardo Gutierrez[5], Bettina Martinez-Hackert[6], Paolo Papale[1]

[1]Istituto Nazionale di Geofisica e Vulcanologia, Via di Vigna Murata 605, 00143 Rome, Italy

[2]Dipartimento di Scienze della Terra, Sapienza-Università di Roma, P.le Aldo Moro 5, 00185 Roma, Italy

[3]Department of Earth Sciences, Institute of Geochemistry and Petrology, ETH, 8092 Zurich, Switzerland

4Department of Earth Sciences, Durham University, Science Site, DH1 3LE, UK

[5]Observatorio ambiental, Ministerio de Medio Ambiente y Recursos Naturales, El Salvador

[6]SUNY Buffalo State, Department of Earth Sciences and Science Education, Buffalo, USA,

Corresponding author:

Silvio Mollo

Sapienza-Università di Roma

Dipartimento di Scienze della Terra

P.le Aldo Moro 5

00185 Roma, Italy

e-mail silvio.mollo@uniroma1.it

Abstract

On December 29, 2013, an isolated vulcanian-type eruption occurred at Chaparrastique volcano (El Salvador) after 12 years of inactivity. The eruption was classified as VEI 2 and produced an ash plume with a maximum height of ~9 km. Textural and compositional data from phenocrysts from the erupted products have been integrated with geochemical and isotopic information from bulk rocks to elucidate the magmatic processes responsible for the reawakening of volcanic activity.

Phenocrysts consist of Fo-rich poikilitic olivines hosting high-Mg titanomagnetites, and Fo-poor olivines coexisting with low-Mg titanomagnetites. Mineral-melt equilibria suggest an origin for the distinct phenocryst populations by mixing between a high-*T* (~1,130-1,150 °C), basaltic magma with fO_2 (NNO buffer) typical of the lower crust in arc systems and a low-*T* (~1,060-1,080 °C), basaltic andesitic magma with fO_2 (NNO+1 buffer) commonly encountered in shallower, more oxidized crustal reservoirs. Thermobarometry based on Fe-Mg exchange between orthopyroxene and clinopyroxene constrains the crystallization before eruption at relative low-*P* (~150-250 MPa) and low-*T* (~1,000-1,050 °C). Mixing between two chemically distinct magmas is also evidenced by the occurrence of reverse zoned plagioclase phenocrysts with resorbed sodic cores and re-growth of sieve-textured calcic mantles. Conversely, plagioclase rims exhibit disequilibrium compositions addressed to decompression kinetics (~10^{-3} MPa/s) driven by rapid magma ascent to the surface (~0.03 m/s).

Major and trace element modelling excludes fractional crystallization as the primary mechanism controlling the bulk rock variability, whereas geochemical data align along a mixing trend between two end-members representative of the primitive basalt and the differentiated basaltic andesite. Trace element and isotope data indicate that the primary source of magmatism is an enriched MORB-like mantle with the contribution of fluxes of metasomatic fluids and/or melts produced by the subducted slab. The role played by slab-fluid inputs of carbonate origin and slab-melts from the hemipelagic sediments seems to be minimal. Assimilation/contamination processes

of magmas by crustal rocks are also negligible. In contrast, the geochemical signature of magmas is greatly influenced by slab-derived aqueous fluids produced prevalently by progressive dehydration of marine sediments and altered basaltic crust.

Keywords: Chaparrastique volcano; Central American volcanic arc; magma mixing; magma decompression;

1. Introduction

El Salvador is one of the most seismically-active regions on Earth (Fig. 1a), being located along the Central American volcanic front that is defined by ~50 major volcanic centers, including composite or clustered volcanoes, distributed nearly continuously along 1,200 km from western Guatemala to central Panama (e.g., Carr et al., 1979; Carr, 1984; MacMillan et al., 2004). The Volcanic Cordillera in El Salvador is a line of volcanoes parallel to the coast and the offshore subduction zone. El Salvador has 23 volcanoes and 5 volcanic fields. At present, only a few volcanoes are active (outgassing and rarely ash emissions) such as the Santa Ana, San Salvador, San Miguel and Izalco volcanoes (e.g., Agostini et al., 2006 and references therein).

Chaparrastique volcano, also known as San Miguel, is a composite volcano in central-eastern El Salvador, ~15 km southwest of the city of San Miguel. A rural population of ~70,000 people live within 10 km of the summit crater of Chaparrastique, and San Miguel is the second largest city in El Salvador. On December 29, 2013, after 12 years of inactivity, Chaparrastique volcano erupted at 10:30 local time (16.30 GMT), prompting the evacuation of more than ~5,000 people living in ~3 km radius around the volcano (Martinez-Hackert et al., 2015). The eruption was a vulcanian-type explosion that lasted 2.5 hours (Fig. 1b). The explosion was classified as VEI 2 and produced an ash plume with a maximum height of ~9 km (Martinez-Hackert et al., 2015). The eruption column generated heavy ash fall in nearby areas downwind, especially in the towns of Chinameca and San Jorge. A short lived pyroclastic density current generated from an early Vulcanian explosion travelled ~500 m down the flanks of the volcano and entered coffee plantations.

On January 2014, in response to a request of support by the government of El Salvador, the INGV (Istituto Nazionale di Geofisica e Vulcanologia, Italy) organized a task force in close collaboration with volcanologists from MARN (Ministerio de Medio Ambiente y Recursos Naturales, El Salvador). A campaign survey was conducted over a period of ten days, with the aim to install a monitoring network on the flanks of the volcano (Bonforte et al., 2015; Granieri et al.,

105 2015; Scarlato et al., 2014). At the same time, a suite of twelve eruptive products (i.e., fallout
106 tephra) was collected in correspondence of the seismic monitoring stations of VSMG, RANC, and
107 LACA located, respectively, at 1 km north, 2 km east, and 3 km south-east to the crater (Fig. 1c).
108 Here we present textural and mineral chemistry data from phenocrysts integrated with bulk
109 rock geochemical and isotopic data, with the aim to elucidate magmatic processes that triggered the
110 2013 eruption. Mineral-melt equilibria, and major and trace element modelling define the pre-
111 eruptive crystallization conditions of the system and indicate that magma mixing and magma
112 decompression were the most important mechanisms for triggering the eruption. The magma source
113 has been also constrained by trace element and isotope systematics. Magmas were generated by
114 partial melting of an enriched MORB-like mantle wedge with a dominant contribution of aqueous
115 fluids derived from the subducted slab.
116

117 ## 2. Geological setting

118 The Pacific coastline of much of Central America is marked by a line of active and quiescent
119 volcanoes known as the Central American Volcanic Arc (CAVA) (e.g. Aubouin et al. 1982; Carr et
120 al. 1990, 2004; Leeman et al. 1994; Protti et al. 1995). To the south of Central America the Cocos
121 Plate, which underlies an area of the east Pacific, is being subducted beneath the Caribbean Plate
122 along the Middle American trench. The volcanoes result from the upward movement of magma
123 generated along the subduction zone between the Cocos and Caribbean tectonic plates. El Salvador,
124 and neighbouring Central American states, lies on the Caribbean Plate. Frequent earthquakes also
125 occur along the plate boundary. From Guatemala to northern Costa Rica, ~25 Ma old crust (formed
126 at the East Pacific Rise) is subducted at an angle varying from 55° in Guatemala and El Salvador to
127 65° in Nicaragua and northern Costa Rica (Protti et al. 1995; Syracuse and Abers 2006). The crustal
128 thickness, angle of subduction, and convergence rate contribute to the thermal structure of the
129 subduction zone, which is a major control on the generation of magmas in Central America (Davies
130 and Stevenson, 1992). The sediment input consists of a ~200-m-thick layer of hemipelagic clay

overlying a ~250-m-thick layer of carbonate ooze (Aubouin et al. 1982; Plank and Langmuir 1998). The calc-alkaline compositions of volcanic rocks from CAVA record systematic along-strike variations in many geochemical tracers of the slab, including Ba/La (Carr et al., 1990), U/Th (Patino et al., 2000), B/Be (Leeman et al., 1994), and $\delta^{18}O$ (Eiler et al., 2005). For most of these tracers, the peak in inferred slab flux occurs in the central portion of the CAVA, in Nicaragua, and falls to nearly the global minimum to the southeast, at the terminal sector of volcanoes of Costa Rica. Where the crust is thinner, high-Mg basalts are more abundant (e.g., Nicaragua). Conversely, in correspondence of a thick and old continental crust, low-Mg basaltic lavas occur and are less abundant (e.g., central and western Guatemala). Moreover, the continental crust of southern Central America is relatively young and thin, compared to the crust of other continental margins, making it less radiogenic (Carr 1984; Donnelly et al. 1990).

Chaparrastique volcano in eastern El Salvador is a 2,130 m-high symmetrical stratovolcano with a broad, deep crater complex, which has frequently changed morphology during historic eruptions (Escobar, 2003). Chaparrastique is considered one of the most active volcanoes in El Salvador, with 26 eruptions in the past 500 years. Seismic activity is high, while surface activity consists of pulsating gas emissions that ascend to maximum heights of ~200 m. On December 29, 2013, the volcano erupted ~80 vol.% of crystal-free juvenile material (shards of fresh glass and crystal fragments) associated with ~20 vol.% of lapilli and scoria clasts. The eruption formed a new spatter cone in the central crater. In the days that followed, the SO_2 emissions were estimated to reach 2,800 tons per day. The increasing tremor and gas emissions also suggested migration of hot fluids (gas, water, and magma) into the shallow plumbing system of the volcano. Before such event, the eruptive history of Chaparrastique was characterized by the occurrence of modest VEI 1–2 eruptions (search for Chaparrastique at the MARN's webpage http://www.marn.gob.sv), mainly attributed to spattering and scoria cones at the flanks, and minor Strombolian and ash eruptions in the summit crater (Chesner et al., 2004). Since the 29 December eruption, Chaparrastique has experienced periods (from May to July 2014) of increased seismic and degassing activity, landslides

inside the crater, and lahars. Occasionally, small steam/phreatomagmatic explosions and minor ash falls have occurred, but no substantial explosive events have been reported. However, the level of alert remains high and explosions of small to moderate size similar to the 29 December event remain a possibility.

3. Methods

Textural and microchemical analyses were carried out at the HP-HT Laboratory of Experimental Volcanology and Geophysics of the Istituto Nazionale di Geofisica e Vulcanologia in Rome (Italy). Images were collected using the backscattered electron (BSE) mode of a field emission gun-scanning electron microscopy (FE-SEM) Jeol 6500F equipped with an energy-dispersive spectrometer (EDS) detector. Microchemical analyses were performed using an electron probe micro-analyzer (EPMA) Jeol-JXA8200 combined EDS-WDS (five spectrometers with twelve crystals) with 15 kV accelerating voltage and 10 nA electric current. For glasses, a slightly defocused electron beam with a size of 3 μm was used, with a counting time of 5 s on background and 15 s on peak (Table 1S). For crystals, the beam size was 1 μm with a counting time of 20 and 10 s on peaks and background, respectively (Table 1S). The following standards have been adopted for the various chemical elements: jadeite (Si and Na), corundum (Al), forsterite (Mg), andradite (Fe), rutile (Ti), orthoclase (K), barite (Ba), apatite (P), spessartine (Mn) and chromite (Cr). Sodium and potassium were analyzed first to prevent alkali migration effects. The accuracy of the microprobe was measured through the analysis of well-characterized synthetic oxides and mineral standards. Data quality was ensured by analyzing these test materials as unknowns. Based on counting statistics, analytical uncertainties relative to their reported concentrations indicate that precision was better than 5% for all cations.

Bulk rock analyses for major and trace elements, as well as oxygen isotope analyses were conducted at Actlabs (Activation Laboratories Ltd.). These analyses are reported in the supplementary material (Table 2S), together with measured and certified analyses of international

reference materials. Major elements were analyzed by lithium metaborate/tetraborate fusion – ICP-OES (inductively coupled plasma optical emission spectrometry). Sample washing was performed to remove any organic, loosely adhered, and cementing material. Washing included soaking in a hot mixture of HCl and H_2O_2 as well as cleaning in acetone using ultrasound. The analyses were performed in a batch system. Each batch contained a method reagent blank, certified reference material and 17% replicates. Samples were mixed with a flux of lithium metaborate and lithium tetraborate and fused in an induction furnace. The molten material was immediately poured into a solution of 5% nitric acid containing an internal standard, and mixed continuously until completely dissolved (about 30 minutes). The samples were run on a Thermo Jarrell-Ash ENVIRO II ICP. Calibration was performed using 7 prepared USGS and CANMET certified reference materials. FeO was determined through titration, using a cold acid digestion of ammonium metavanadate, and hydrofluoric acid in an open system. Ferrous ammonium sulphate was added after digestion and potassium dichromate was the titrating agent. This cold digestion dissolved silicates and some sulphides. Water content was determined by gravimetric method. About 0.3 g sample was thermally decomposed in a resistance furnace in a pure nitrogen environment at 110 °C (moisture, H_2O^-) followed by decomposition at 1,000 °C (interstitial water, H_2O^+), using an ELTRA CW-800, directly releasing H_2O. Trace elements were measured by lithium metaborate/tetraborate fusion – ICP-MS (inductively coupled plasma mass spectrometry). Samples fused as reported above were diluted and analyzed by Perkin Elmer Sciex ELAN 6000, 6100 or 9000 ICP/MS. Three blanks and five controls (three before sample group and two after) were analyzed per group of samples. Oxygen isotopes are measured by reaction with BrF5 at about 650 °C in nickel bombs. The fluorination reaction converts O in the minerals to O_2 gas, which is subsequently converted to CO_2 gas using a hot C rod. All reaction steps are quantitative. Bulk rock isotopic analyses are performed on a Finnigan MAT Delta, dual inlet, isotope ratio mass spectrometer. The data are reported in the standard delta notation as per mil deviations from V–SMOW (hereafter reported to as SMOW). External reproducibility is ±0.19‰ (1 s).

The isotopic compositions of Sr and Nd (Table 2S) were measured at the ETH Zürich using a Triton Plus thermal ionization mass spectrometer (TIMS). Details of analytical techniques, accuracy and precision can be found in von Quadt (1997). The isotope analysis set for Sr and Nd was performed on bulk rock powder (50–100 mg). Values for $^{87}Sr/^{86}Sr$ were internally corrected for fractionation using a $^{88}Sr/^{86}Sr$ value of 8.37521. Repeated measurements of the NBS 987 standard for $^{88}Sr/^{86}Sr$ gave a mean value of 0.710252 ± 0.000002 (2σ). $^{143}Nd/^{144}Nd$ values were internally corrected for mass fractionation using a $^{146}Nd/^{144}Nd$ value of 0.7219. No correction on Nd was performed due to good segregation of Nd and Sm during column chemistry. Repeated measurements on the Nd Merck standard for $^{146}Nd/^{144}Nd$ gave a mean value of 0.511730 ± 0.000001 (2σ). The analytical uncertainties associated to the Sr and Nd isotopic compositions of our samples are in the range of 0.000006-0.000019 and 0.000002-0.000012, respectively.

4. Mineralogy, petrology and geochemistry

Mineral chemistry, petrology and geochemistry was performed in twelve samples of juvenile material and scoria clasts ejected during the 2013 eruption. The juvenile material consists of white-grey coarse ashes and dark-grey accretionary lapilli (i.e., CH1, CH2, CH4, CH5, CH8, CH10, CH11, and CH12 samples), and are associated to centimetre-sized scoria clasts containing phenocrysts and microlites surrounded by matrix glass (i.e., CH3, CH6, CH7, and CH9 samples). Mineral and matrix glass analyses of scoria clasts are reported in Table 1S submitted as supplementary material. Bulk rock analyses of the juvenile material and scoria clasts are reported in Table 2S submitted as supplementary material. Major and trace elements were measured for all the bulk rock samples, whereas radiogenic and stable isotopes were analyzed only for CH1, CH2, CH4, CH9, and CH12 samples that represent the entire bulk rock compositional variation.

4.1 Textures of scoria clasts

The paragenesis of scoria clasts is dominated by phenocrysts of olivine and plagioclase (~23 vol.%), and minor pyroxene and spinel (~7 vol.%). The groundmass consists of plagioclase, pyroxene, and spinel microlites (~12 vol.%), surrounded by matrix glass (~58 vol.%). The relatively low microlite content suggests that, at the time of eruption, late crystallization was hampered by rapid quenching of magma.

The habit of olivine is generally euhedral with well-formed planar edges. Larger olivine phenocrysts are poikilitic and enclose sub-rounded spinels (Fig. 2a), whereas smaller olivines are accompanied by spinel phenocrysts with irregular boundaries and glass embayments resulting from the agglomeration of bleb-like grains (Fig. 2b).

Pyroxene crystallized as both sub-euhedral orthopyroxene and clinopyroxene. Orthopyroxenes are less frequently observed but sometimes occur as large phenocrysts partly enclosing small clinopyroxenes (Fig. 2c).

Plagioclase is characterized by complex zoning in which the cores, mantles and rims are separated by sharp interfaces. BSE images reveal (1) dark-grey, partly corroded cores, (2) light-grey, coarsely sieve-textured mantles, and (3) grey, euhedral to sub-euhedral rims (Fig. 2d-f). Notably, detailed BSE images of the plagioclase rims show that their final euhedral habit results from the attachment of a number of groundmass microlites growing as tabular crystals (Fig. 2g-i). These small, elongated plagioclases attach preferentially parallel preferentially parallel to the longest crystal dimension that normally corresponds to the [100] crystallographic direction contributing to the textural maturation of the rim. In contrast, plagioclase mantles are characterized by the occurrence of micrometre-sized glass channels and hollows, sometimes, in full communication with the matrix glass when the growth of the crystal rim results incomplete.

4.2 Mineral and glass chemistry of scoria clasts

Olivine is normally zoned with forsterite (Fo) contents decreasing from core-to-rim. Larger poikilitic olivines enclosing spinels show Fo_{77-78} cores and Fo_{74-76} rims (Fig. 2a). The olivine core is

also more calcic (0.51-0.63 wt.% CaO) than the rim (0.32-0.56 wt.% CaO). Conversely, smaller olivines mutually touching with spinels in the matrix glass are weakly zoned with Fo_{74-75} cores and Fo_{72-73} rims (Fig. 2b).

Spinel is titanomagnetite with variable ulvospinel content (Usp). Smaller, sub-rounded titanomagnetites enclosed in olivine are Usp_{24-27} (Fig. 2a), whereas single, isolated titanomagnetites are Usp_{21-19} (Fig. 2b). Titanomagnetites in poikilitic olivines are also more primitive (~6-7 wt.% MgO) than those found in the matrix glass (~4-5 wt.% MgO).

Pyroxene is both orthopyroxene and clinopyroxene. Orthopyroxene exhibits weak chemical variation with a narrow enstatite (En) content of En_{60-63} (Fig. 2c). Clinopyroxene is augite (cf. Morimoto et al., 1988) with relative low-CaO concentration (<17 wt.%) and variable diopside (Di) content ranging from Di_{37} to Di_{46} (Fig. 2c).

Among all the minerals, plagioclase phenocrysts are characterized by important compositional changes reflecting the complex textural characteristics. Plagioclases are strongly reversely zoned with resorbed sodic cores surrounded by dusty sieve-textured calcic mantles. This suggests an origin by resorption and rapid re-growth due to mixing between two compositionally distinct magmas. The anorthite (An) content sharply increases from core (An_{53-65}) to mantle (An_{80-84}). Conversely, at the final stage of the crystal growth, a thin-to-thick rim occurs with chemistry (An_{77-80}) intermediates between core and mantle compositions (Fig. 2d, e, f). Importantly, the rim chemistry is almost identical to that of groundmass plagioclases, suggesting coeval crystallization (Fig. 2g, h, i).

The matrix glass is 52.7-54.3 wt.% SiO_2 and 3.5-4.6 wt.% Na_2O+K_2O, corresponding to the composition of a basaltic andesite (i.e., Le Bas et al., 1986). However, Mg# (100 × molecular $MgO/FeO_{tot} + MgO$) values are highly variable ranging from 25 to 43. Indeed, the glass analyses are not homogeneous showing concentration gradients especially next to the well-developed rims of large plagioclase phenocrysts (see discussion below). Within such chemical variability, the

285 composition of the matrix glass does not differ substantially from that of micrometre-sized glass
286 channels and glass inclusions within plagioclase phenocrysts.
287
288 4.3 Bulk rock geochemistry
289 On anhydrous basis, the products are calc-alkaline basalts (CH1-CH2) and moderately
290 (CH3-CH6) to more differentiated (CH7-CH12) basaltic andesites (i.e., Le Bas et al., 1986; Fig. 3a)
291 with medium-K affinity (i.e., LeMaitre, 2002; Fig. 3b). Bulk rocks align along one single trend in
292 which both silica and alkali explore limited compositional variations (Fig. 3a-b). From CH1 to
293 CH12, MgO and CaO linearly decrease from ~7 to ~3 wt.% and from ~11 to ~8 wt.%, respectively,
294 reflecting the more evolved character of the samples.
295 The chondrite-normalized pattern (Sun and McDonough, 1989) of REE (rare earth elements;
296 Fig. 3c) exhibits sub-parallel trends shifting towards progressive REE enrichments from CH1 to
297 CH12. Slight enrichments in LREE (light rare earth elements) relative to HREE (heavy rare earth
298 elements) are also observed. Bulk rocks are characterized by weak negative Eu anomaly (Eu/Eu* =
299 0.86-0.92) and relatively low values of normalized La/Yb ratios (2.8-3.1). The primordial mantle-
300 normalized pattern (Sun and McDonough, 1989) of trace elements (Fig. 3d) shows typical features
301 of arc magmas, with LILE (large ion lithophile elements) to HFSE (high field strength elements)
302 ratios higher than the primitive mantle values. This is confirmed by low Nb and Ta concentrations
303 and correspondingly high Ba/Ta (2,900-4,200) and La/Ta (62-80) ratios. The incompatible elements
304 generally increase with increasing SiO_2. Moreover, trace element patterns show positive spikes of
305 Ba, U, K and Sr, and negative Nb, Ta, Ti, Hf and Zr anomalies. The compatible TE (transition
306 elements) such as Ni (11-20 ppm) and Cr (20-58) are low and their concentration decreases from
307 CH1 to CH12, in accordance with decreasing MgO.
308 Radiogenic isotope compositions of bulk rocks are constrained in narrow intervals of
309 0.70377-0.70387 and 0.51291-0.51299 for $^{87}Sr/^{86}Sr$ and $^{143}Nd/^{144}Nd$ ratios, respectively. According
310 to isotope data from other volcanoes in El Salvador, the lack of sensible isotopic variations with the

311 degree of magma evolution indicates that crustal contamination processes are likely to be minimal
312 (Agostini et al., 2006).

313 Oxygen-isotope ratios range between 5.4 and 5.6 ‰, showing values comparable to most
314 mantle peridotites (~5.5 ± 0.2‰; e.g., Mattey et al., 1994). However, it is important to note that the
315 oceanic lithosphere is highly heterogeneous in $\delta^{18}O$ and may contribute with slab-derived
316 components with oxygen-isotope ratios (0-6‰) equal to or lower than typical upper mantle
317 peridotites, i.e., hydrothermally altered lower oceanic crust and ultramafic rocks such as
318 serpentinites (Cocker et al., 1982; Staudigel et al., 1995).

319

320 ## 5. Discussion

321 5.1 Magma crystallization conditions

322 In order to decipher the crystallization conditions of the erupted products, the olivine-based
323 thermometer of Putirka (2005a) with a relatively low uncertainty of ±27 °C has been used. Olivine-
324 melt equilibria are particularly useful for temperature estimations because the Fe-Mg exchange
325 reaction is nearly constant over a wide range of temperatures, bulk compositions and fO_2 conditions
326 (i.e., $^{ol\text{-}melt}Kd_{Fe-Mg}$ = 0.30 ± 0.03), and because the olivine Fo content is highly sensitive to the
327 thermal path of magma (e.g., Roeder and Emslie, 1970). Assuming that olivine is the liquidus phase,
328 its early-formed core is expected to be in equilibrium with the original magma represented by the
329 bulk rock analysis (cf. Putirka 2008). Through this approach, it is found that Fo_{78-77} olivines are in
330 equilibrium with the primitive basalts (MgO > 6 wt.%), yielding onset temperatures of 1,135-
331 1,146 °C (Fig. 4a). Conversely, Fo_{74-75} olivines are in equilibrium with the more evolved basaltic
332 andesites (MgO < 4 wt.%), recording onset temperatures of 1,067-1,084 °C (Fig. 4a). The
333 equilibrium condition is attained when the total Fe of the melt is partitioned between Fe^{2+} and Fe^{3+}
334 through the formulation of Kress and Carmichael (1991), over buffering conditions relative to NNO
335 (nickel-nickel oxide) and NNO+1, respectively for Fo_{78-77} and Fo_{74-75} olivines. These different redox
336 states have been predicted by the spinel-melt oxygen barometer of Ariskin and Nikolaev (1996),

using high-Mg titanomagnetites hosted in Fo_{78-77} poikilitic olivines (Fig. 2a) and low-Mg titanomagnetites coexisting with Fo_{74-75} olivines (Fig. 2b). The distinct textural and chemical characteristics for olivine and titanomagnetite suggests mixing between a high-*T*, mafic melt with fO_2 typical of the lower crust of volcanic arcs (Brounce et al., 2014) and a low-*T*, differentiated melt with fO_2 commonly encountered in shallower, slightly more oxidized crustal reservoirs (see below).

With respect to plagioclase crystallization, the equilibrium model of Namur et al. (2012) indicates that the more sodic (An_{53-65}) core and the more calcic (An_{80-84}) mantle approach to equilibrium with more evolved (CaO ≤ 8 wt.%) and primitive (CaO ≥ 9 wt.%) bulk rocks, respectively (Fig. 4b). Conversely, the equilibrium condition is never found between the intermediate (An_{77-80}) plagioclase rim and the overall bulk rock compositions. The plagioclase rim is also in disequilibrium with the surrounding matrix glass (Fig. 4b) and data deviate from the one-to-one straight line, responding to moderate An enrichments in the plagioclase rim (ΔAn = 16-27%). The thermometer of Putirka (2005b) with uncertainties of ±36 °C, yields crystallization temperatures of 1,051-1,063 °C, 1,119-1,129 °C, and 1,098-1,117 °C for plagioclase core, mantle and rim, respectively. These predictions account for minimum H_2O-melt concentration of 2 wt.% derived by the difference to 100% of the total of electron microprobe analyses of matrix glasses (cf. Devine et al., 1995). It has been also tested that H_2O contents up to 4 wt.% changes the temperature estimates by ±32 °C that, however, remains within the relatively high uncertainty of the thermometer. The occurrence of low-*T*, partly resorbed cores surrounded by high-*T*, sieve-textured mantles (ΔT ~70 °C) confirms mixing between two compositionally distinct magmas. It is therefore inferred that a colder, basaltic andesitic magma reservoir was intruded by a hotter, basaltic magma rising from depth. The increase in An content for the plagioclase mantle supports the hypothesis that the new magma was compositionally more primitive and possibly hotter and/or wetter. The textural evidence of dissolution and patchy regions at the inner part of the plagioclase corroborates the mixing mechanism (e.g., Tsuchiyama and Takahashi, 1983; Tsuchiyama, 1985; Tepley et al., 2000). Therefore, more evolved Fo_{74-75} olivines and An_{53-65} plagioclases crystallized from a colder

363 basaltic andesitic magma that, subsequently, mixed with the hotter basaltic magma rising from
364 depth and carrying more primitive Fo_{78-77} olivines. Pre-existing less calcic An_{53-65} plagioclases in
365 contact with the recharging basaltic magma experienced an increase in temperature that resulted in
366 resorption textures (Fig. 3d-f). While the recharging and host magmas attempted to hybridize, high-
367 temperature gradients lead to relatively rapid crystallization of sieve-textured, more calcic An_{80-84}
368 mantles with the contribution of the more primitive component of the mixing system (e.g., Hibbard,
369 1981; Shcherbakov et al., 2010). Coherently with this scenario, the weak negative europium
370 anomaly of the bulk rocks excludes substantial plagioclase fractionation at depth (Fig. 3c).
371 By means of the two-pyroxene model of Putirka (2008), it is found that orthopyroxene and
372 augite exhibit Fe-Mg exchange values (i.e., $^{cpx\text{-}opx}Kd_{Fe-Mg}$ = 1.09 ± 0.14; Fig. 4c, d) indicative of
373 equilibrium crystallization from the hybrid magma from which pyroxenes formed immediately
374 before eruption. Temperature and pressure estimates based only on mineral chemistry (i.e.,
375 independently on melt composition) provide values of 1,012-1,053 °C (uncertainty of ±38 °C) and
376 158-253 MPa (uncertainty of ±200 MPa), respectively (Fig. 4c-d). The temperature estimates are
377 lower than those obtained for the more evolved Fo_{74-75} olivine and An_{53-65} plagioclase, evidencing a
378 late stage of pyroxene crystallization from the more oxidized hybrid magma. According to Grove
379 and Juster (1989), if fO_2 of calc-alkaline magmas increases to NNO+1, the crystallization of
380 orthopyroxene + augite occurs at the expense of pigeonite (never observed in samples from this
381 study) along a single reaction boundary in which olivine + liquid = orthopyroxene + augite +
382 plagioclase. In addition, the formation of a clinopyroxene with relative high-Ca contents is also
383 limited by previous incorporation of Ca in plagioclase.
384 Considering the wide spectrum of equilibrium experiments from the literature, the calc-
385 alkaline melts studied by Foden and Green (1992) show compositions comparable to those from
386 this study. At $P \geq 500$ MPa and $H_2O < 2$ wt.%, plagioclase is the liquidus phase followed by olivine
387 or, alternatively, pyroxene if $P \geq 700$ MPa. However, at $P \geq 500$ MPa and $H_2O \geq 2$ wt.%, the
388 stability field of liquidus olivine expands significantly, so that plagioclase does not crystallize from

389 the melt. On the other hand, at P = 200 MPa and H_2O = 2-4 wt.%, the crystallization sequence
390 consists of olivine, olivine + plagioclase, and olivine + plagioclase + pyroxene (Fig. 5). This latter
391 phase assemblage closely agrees with the textural relationships and saturation temperatures of
392 natural minerals from this study, evidencing primary nucleation and growth of olivine + plagioclase,
393 and subordinated formation of pyroxene. The lack of amphibole in the eruptive products is also in
394 accordance with a low-P crystallization path in which the amphibole saturation surface is
395 encountered only at T < 950 °C (Fig. 5).

396 Generally, El Salvador arc lavas crystallize at $P \leq 500$ MPa, NNO-NNO+1 buffer, and 3–4
397 wt.% H_2O (Agostini et al., 2006). The shallow residing conditions of magmas are corroborated by
398 the low La/Yb ratios of bulk rocks, excluding development of large magma chambers in a thick
399 crust with HREE-bearing minerals. Moreover, melt-H_2O contents of 2-4 wt.% are frequently
400 documented for arc magmas in Central America (e.g., Sisson and Layne, 1993; Roggensack et al.,
401 1997; Roggensack, 2001), accounting for the remarkable fluid contribution to the mantle wedge
402 from the subducting slab (e.g., Patino et al., 2000). Wade et al. (2006) observed that the correlation
403 between melt-H_2O contents and Ba/La ratios may be significant. On this basis, Sadofsky et al.
404 (2007) proposed a regression fit in which the ratio of Ba/La can be used as a proxy for H_2O in
405 magma. Through this equation it is determined that Ba/La ratios of bulk rocks from this study
406 correspond to original melt-H_2O contents of 3.3-3.7 wt.%, coherently with previous estimates for El
407 Salvador arc lavas by Agostini et al., (2006), and the low-P crystallization sequence experimentally-
408 derived by Foden and Green (1992). Notably, LOI (Loss-On-Ignition) from bulk rock analyses
409 (Tables 2S) ranges from 1.1-2.1 wt.% (considering total iron as FeO) suggesting overall outgassing
410 of magma during eruption to the surface and pressure drops down to atmospheric condition (Aloisi
411 et al., 2006; Toramaru et al., 2008; Rutherford, 2008; Gonnermann and Manga, 2013).

412

413 5.2 Magma mixing vs. magma fractional crystallization

Magma mixing is recognized as a widespread process in calc-alkaline, arc-related magmas that contributes to magma chamber evolution and is a likely trigger for eruptions (Sparks et al. 1977; Eichelberger et al. 2000). Previous petrological studies on volcanoes along the CAVA have documented the role of magma mixing as the cause of substantial changes in major and trace element compositions (e.g., Streck et al., 2002; Richer et al., 2004). In particular, magma mixing has been observed for a number of volcanoes in El Salvador, generally between basaltic andesitic and andesitic magmas (e.g., San Vincente volcano), and between basaltic andesitic and rhyodacitic magmas (e.g., Ilopango volcano), leading to a variety of complex rock textures characterized by corroded/resorbed plagioclases and bimodal compositional distributions of phenocrysts (e.g., Carr et al., 2007 and references therein).

If magma mixing occurred at the time of Chaparrastique eruption, bulk rock compositions are expected to plot on tie-lines between CH1 and CH12 end-members, resulting to be rather different from the curved trajectories caused by fractional crystallization. To test this hypothesis, MELTS (Ghiorso and Sack, 1995) simulations have been conducted using the most primitive CH1 basalt as a starting liquid (Table 3s submitted as supplementary material). Thermodynamic runs started from the superliquidus temperature of 1,170 °C and continued along a fractional crystallization path that terminated at 1,020 °C. The pressure, melt-H_2O content and oxygen fugacity were set at 200 MPa, 3 wt.%, and NNO+1, respectively, as the best input parameters reproducing the natural phase assemblage. Results show that the curved MELTS trajectories do not match in full with the natural Chaparrastique compositions that, in turn, align along tie-lines between CH1 and CH12 end-members (Fig. 6a). This is also true for the behaviour of trace elements modelled by the Excel spreadsheet of Ersoy and Helvaci (2010). The original partition coefficients set in the spreadsheet were used to derive the fractional crystallization vectors for REE (Fig. 6b), HFSE (Fig. 6c), and TE (Fig. 6d). While these vectors describe an implausible magmatic evolution for the Chaparrastique products, the bulk rock variability is successfully modelled by mixing (straight) lines joining CH1 and CH12 end-members (Fig. 6b-d).

440

441 5.3 Magma decompression and ascent to the surface

442 Plagioclase phenocrysts from Chaparrastique eruption exhibit partly resorbed An_{53-65} cores that are
443 the herald of early equilibrium in a basaltic andesitic magma chamber, and sieve-textured An_{80-84}
444 mantles interpreted as markers of further basaltic recharge (Fig. 2d, e, f and Fig. 4b). If the mixing
445 efficiency is low, the influx of mafic magma, possibly transferring heat and H_2O, causes inverse
446 zoning of plagioclase due to dissolution and overgrowth of highly calcic crystals (e.g., Tsuchiyama
447 1985; Davidson and Tepley 1997). Conversely, if the system rapidly re-equilibrates to form a
448 homogeneous hybrid melt, an overall normally zoned trend is resumed with newly-formed calcic
449 cores grading into sodic rims (e.g., Izbekov et al. 2004; Neill et al., 2015). Apparently, this latter
450 mechanism seems to explain the final growth of An_{77-80} plagioclase rims and the crystallization of
451 groundmass microlites (Fig. 3d-i). However, these late-stage plagioclases are not in equilibrium
452 with the hybrid melt if its composition is assumed to correspond with the final matrix glass (Fig.
453 4b). Moreover, chemical profiles carried out far enough away from the plagioclase surface reveal
454 that the matrix glass is not homogeneous (Table 4s), due to the development of chemical gradients
455 at the crystal-melt interface (Fig. 7a).

456 Numerous cooling and decompression studies explored the effect of magma mixing and
457 undercooling on the crystallization kinetics of plagioclase (e.g., Kirkpatrick et al., 1976; Smith &
458 Lofgren, 1983; Muncill & Lasaga, 1987; Sato, 1995; Hammer & Rutherford, 2002; Couch, 2003;
459 Pupier et al., 2008; Fiege et al., 2015). According to experimentally-derived data (Mollo et al., 2011,
460 2012a), if crystal growth rate is large compared with the rate of component diffusion in the melt, a
461 diffusive boundary layer develops causing enrichments in elements incompatible with the
462 plagioclase crystal lattice (Fig. 7a). Concentration–dependent partitioning produces plagioclases
463 that respond to chemical gradients in the melt, so that crystals incorporate high Ti, Mg, and Fe
464 proportions (Fig. 7a) and become preferentially enriched in An with respect to equilibrium
465 crystallization (Fig. 4b). The effect of undercooling due to temperature decrease (cf. Mollo et al.,

2011) and/or H_2O exsolution (cf. Brugger & Hammer, 2010) leads to the formation of disequilibrium An-rich plagioclases in response to the drastic change of the topology of the Ab-An plagioclase binary loop in which the temperature difference between liquidus and solidus is minimized (cf. Iezzi et al., 2014). It is interesting to note that disequilibrium plagioclases crystallizing from rapidly decompressed calc-alkaline melts in laboratory show An enrichments (ΔAn = 12-30%; data from Brugger & Hammer, 2010) very close to those (ΔAn = 16-27%) measured in this study. The control of undercooling is also evidenced by the attachment of groundmass microlites to form the plagioclase rim (Fig. 3g-i). This crystal growth mechanism has been documented under kinetically-controlled conditions by in-*situ* experimental observations (Schiavi et al., 2009), crystal size distribution analysis (Iezzi et al., 2011; Lanzafame et al., 2013), and electron-microprobe mapping (Iezzi et al., 2014). The attachment mechanism is possibly explained by heterogeneous nucleation events on the pre-existing crystal surface (Mollo et al., 2012b; Vetere et al., 2015) and/or by the emerging theory of aggregation by self-orientation of sub-micrometric crystals (Teng et al., 2013 and references therein).

An important consequence of the diffusion–controlled growth is that the partition coefficient measured between the advancing plagioclase surface and the diffusive boundary layer changes upon the effect of chemical gradients in the melt. The partition coefficient is expressed as:

$$K_i = C_i^{xls} / C_i^{melt} \quad (1)$$

where C_i^{xls} is the concentration of a chemical element *i* in the crystal and C_i^{melt} is the concentration of the same element in the melt. If the compositions of both crystal and melt result from interface–controlled growth and are supposed to be in equilibrium with respect to element exchange at the crystal–melt interface, Eqn. (1) provides the 'true' partition coefficient K_i^{true}. Conversely, the effect of diffusion–controlled growth is to change K_i^{true} in an 'apparent' partition coefficient K_i^{app} when the

chemistry of the advancing crystal surface reflects the chemical concentrations in the diffusive boundary layer. During plagioclase disequilibrium growth driven by undercooling, it has been experimentally-derived that $K_{Fe}^{app} > K_{Fe}^{true}$ and $K_{Mg}^{app} > K_{Mg}^{true}$ (Mollo et al., 2011). For the case of natural plagioclase phenocrysts, the lattice strain equation of Dohmen & Blundy (2014) represents a powerful tool to predict whether or not the partitioning of Mg is controlled by equilibrium or disequilibrium growth conditions. The model was derived by thermodynamic principles and allows to predict K_{Fe}^{true} for a wide range of equilibrium plagioclase and melt compositions. The partitioning of Mg measured between sodic core (or calcic mantle) of plagioclase and CaO-poor (or CaO-rich) bulk rocks yields values close to those predicted by the lattice strain equation of Dohmen & Blundy (2014). It is worth noting that $\ln K_{Mg}$ increases linearly with $1/T$, according to thermodynamic principles of cation partitioning (Fig. 7b). In contrast, partition coefficients measured as the ratio between plagioclase rim and matrix glass show values much higher than those expected for equilibrium crystallization (Fig. 7b), as for the case of $K_{Mg}^{app} > K_{Mg}^{true}$ due to the effect of undercooling (Mollo et al., 2011). If the advancing plagioclase rim does not violate the condition of crystallization into an infinite melt reservoir, the value of K_{Mg}^{app} can be modelled as a function of melt and crystal parameters (Smith et al., 1955):

$$K_{Mg}^{app} = 1/2 \left\{ 1 + erf\left[\sqrt{G^{pl} x / D_{Mg}^{melt}} / 2 \right] \right\} + (2K_{Mg}^{true} - 1) \exp\left\{ \left[-K_{Mg}^{true}(1 - K_{Mg}^{true})(G^{pl} x / D_{Mg}^{melt}) \right] \; erfc\left[(2K_{Mg}^{true} - 1) / 2\sqrt{G^{pl} x / D_{Mg}^{melt}} \right] \right\} \quad (2)$$

where K_{Mg}^{true} is the equilibrium partition coefficient provided by the formulation of Dohmen & Blundy (2014), G^{pl} is the plagioclase growth velocity that is unknown, D_{Mg}^{melt} is the diffusivity of Mg in the melt (i.e., 9×10^{-11} cm^2/s derived by the model of Zhang et al., 2010), and x is the

distance the plagioclase interface moves into the melt (i.e., the linear dimension of the plagioclase rim). Results based on the algebraic rearrangement of Eqn. (2) show that K_{Mg}^{app} measured in this study can be ascribed to rapid plagioclase growth velocities of ~2-7 × 10^{-8} cm/s (Fig. 7b; see also Table 5s for the entire numerical dataset). Decompression-induced crystallization experiments of Brugger & Hammer (2010) have demonstrated that, in calc-alkaline melts, the growth velocity of plagioclase scales with the decompression path of magma (ΔP). It is found that ~10^{-3} MPa/s ΔP corresponds to ~10^{-8} cm/s G^{pl}. If magma decompression started at P = 200 MPa (Fig. 5) over a timescale of ~10^{-3} MPa/s ΔP, the ascent velocity of magma feeding eruption was ~0.03 m/s (i.e., 100 MPa ≈ 3 km), in agreement with values estimated for a number of volcanic eruptions worldwide (Aloisi et al., 2006; Toramaru et al., 2008; Rutherford, 2008; Gonnermann and Manga, 2013; Mollo et al., 2015).

5.4 Magma genesis and slab inputs

While partial melting of the mantle wedge is the predominant source of magmatism in Central America, the geochemical signature of arc magmas is highly influenced by the nature of the subducted slab components (e.g., Carr et al., 2004). An enriched MORB-like mantle has been identified as the primary source for CAVA magmas with the contribution of fluxes of metasomatic fluids and/or melts produced by the crustal units of the subducting Cocos Plate, i.e. the basal altered MORB unit, the middle carbonate unit, and the upper hemipelagic unit (Patino et al., 2000). A generalized approach for identifying the transfer agents between the subducted slab and the mantle wedge is based on the knowledge that ratios of some specific incompatible elements weakly change over the range of mantle melting and/or during assimilation ± fractional crystallization processes. In contrast, the same incompatible element ratios are greatly affected by the contribution of the subducting slab, being distinctive indicators of sediment input into magma genesis (e.g., Cameron et al., 2003).

Considering the different geochemical signature of the hemipelagic and carbonate sediments subducted beneath Central America, the use of U/La and Ba/Th ratios has the advantage to clearly separate the two slab components (Patino et al., 2000). These ratios correspond to soluble/insoluble element pairs with the important feature that U/La is higher in the hemipelagic sediments and Ba/Th is higher in the carbonate sediments (Fig. 8a). Using partition coefficients from literature and the modal batch melting equation, Cameron et al. (2013) modelled the role played by melts and fluids derived from the subducted slab for the partial melting of the enriched MORB source (Fig. 8a). Modelling results indicate that the majority of primitive magmas at the CAVA have relatively low U/La and Ba/Th ratios and cluster near the enriched MORB source. Ba-rich fluids from the carbonate sediments produce magmas with clear slab-fluid signatures (>0.1%) corresponding to high Ba/Th ratios and low U/La ratios observed in Nicaragua and addressed to an increased dip of the subducting Cocos Plate (Patino et al., 2000). In contrast, as the degree of differentiation proceeds, volcanoes in Costa Rica and El Salvador are weakly influenced by slab-fluid inputs of carbonate origin (Fig. 8a). In El Salvador, Ba/Th and U/La ratios of magmas show a low contribution of melts (<0.04%) from the subducted hemipelagic sediments and a relative high participation of fluids (<2%) from the mature oceanic crust (Fig. 8a).

Additional important information concerning the genesis of Central American magmatism can be retrieved by using ratios of elements that are not highly fluid mobile in arc systems, such as REE and HFSE, in order to better evaluate the role of slab components with melt-like properties (Fig. 8b). Volcanic products in Nicaragua form a nearly vertical trend at low La/Sm extending towards the highest Ba/La ratios with respect to other CAVA magmas (Fig. 8b). Taken together with the discussion of Ba/Th and U/La ratios, this finding corroborates the addition to the mantle wedge of variable amounts of Ba-rich fluids derived from subducted carbonate sediments. Conversely, volcanic products in Costa Rica are characterized by the highest La/Sm and La/Yb ratios due to remarkable LREE enrichments (Fig. 8b) but among the lowest Ba/La and Ba/Th ratios, suggesting either involvement of an enriched mantle wedge or a melt-like component derived from

564 the subducted slab (Sadofsky et al., 2007). Volcanic products in El Salvador are intermediate
565 between the geochemical signature of magmas in Nicaragua and Costa Rica, being characterized by
566 relative low La/Sm and moderate Ba/La ratios due to pronounced slab-fluid signals from marine
567 sediments (Fig. 8b).

568 For discriminating between crustal and source contamination of CAVA magmas, Cameron
569 and Walker (2006) modelled the oxygen and strontium isotopes in order to define mixing
570 trajectories between the sediment-modified mantle and crustal end-members (Fig. 8c). For most
571 rocks in Guatemala produced by back-arc volcanism behind the volcanic front, there is clear
572 evidence of crustal contamination (>25%). This accounts for the increased continental crust
573 thickness and the highly radiogenic nature of the old crust (cf. Carr et al., 1990; Walker et al., 1995).
574 In contrast, in Central America, crustal assimilation causes weak changes in the geochemical
575 characteristics of magmas (Fig. 8c). This is particularly true for volcanoes in El Salvador,
576 Nicaragua, and Costa Rica, emplaced in a thin and young continental crust (cf. Eiler et al., 2005)
577 and characterized by magmatism with source contamination signature (<5%).

578 Sr and Nd systematics presented by Cameron et al. (2002) confirm that magmas in
579 Guatemala extend in the direction of high degrees of crust contamination (Fig. 8d). On the other
580 hand, volcanic products in El Salvador, Nicaragua, and Costa Rica define an array with positive
581 slope (Fig. 8d) as the result of a mix between an enriched MORB source and the subducted slab
582 (Feigenson and Carr, 1986; Carr et al., 1990). The slab source itself represents a mix between a
583 depleted MORB source and sediments plus altered basaltic crust (Fig. 8d). Boron isotope data by
584 Tonarini et al. (2007) for El Salvador products acknowledge the importance of slab-derived aqueous
585 fluids as metasomatizing agents of the mantle wedge. These aqueous fluids are mostly produced by
586 dehydration of marine sediments and altered basaltic crust of the subducted slab, but fluxes of
587 additional fluids result also from progressive dehydration of the serpentized mantle wedge dragged
588 beneath the volcanic arc (Tonarini et al., 2007).

589

6. Conclusions

This study documents for the first time the mineralogical, petrological and geochemical characteristics of products erupted at during the 2013 eruption of Chaparrastique volcano. Mineral-melt equilibria and bulk rock modelling indicate that the eruption was likely triggered by the input of hotter, basaltic magma from depth into a colder, basaltic andesitic reservoir residing at shallow crustal levels. Magma mixing is supported by the textural and compositional characteristics of olivine and titanomagnetite reflecting different crystallization histories, as well as by the occurrence of inversely zoned plagioclases showing partly resorbed cores surrounded by sieve-textured mantles. Furthermore, the final growth of plagioclase was controlled by the effect of undercooling due to rapid decompression during magma ascent to the surface. Trace element and isotope data tend to exclude crustal contamination, suggesting that magmas originated by partial melting of an enriched MORB-like mantle wedge metasomatized prevalently by slab-derived aqueous fluids.

Acknowledgments

The authors are grateful to B. S. Ellis, G. Iezzi, and D. B. Dingwell for their useful and constructive suggestions. Francesca Forni and Andrea Cavallo are acknowledge for assistance during sample selection and microprobe analysis, respectively. Part of this work was supported by MIUR project - Premiale NORTh (New hORizons of the Technology applied to experimental researches and geophysical and volcanological monitoring). The research activities of the HP-HT laboratory of the INGV were supported by the European Observing System Infrastructure project (EPOS). RB acknowledges a NERC Urgency Grant (NE/M005003/1).

References

Agostini, S., Corti, G., Doglioni, C., Carminati, E., Innocenti, F., Tonarini, S., Manetti, P., Di Vincenzo, G., Montanari, D., 2006. Tectonic and magmatic evolution of the active volcanic

615 front in El Salvador: insight into the Berlín and Ahuachapán geothermal areas. Geothermics 35,
616 368-408. doi:10.1016/j.geothermics.2006.05.003
617 Aloisi, M., Bonaccorso, A., Gambino, S., 2006. Imaging composite dike propagation (Etna, 2002
618 case). Journal of Geophysical Research 111, B06404.doi:10.1029/2005jb003908
619 Ariskin, A., Nikolaev, G., 1996. An empirical model for the calculation of spinel-melt equilibria in
620 mafic igneous systems at atmospheric pressure: 1. Chromian spinels. Contributions to
621 Mineralogy and Petrology 123, 282-292. doi:10.1007/s004100050156
622 Aubouin, J., Stephan, J., Roump, J., Renard, V., 1982. The middle american trench as an example
623 of a subduction zone. Tectonophysics 86, 113-132. doi:10.1016/0040-1951(82)90063-4
624 Bonforte, A., Hernandez, D., Gutiérrez, E., Handal, L., Polío, C., Rapisarda, S., and Scarlato, P.,
625 2015. The unrest of S. Miguel volcano (El Salvador, CA): installation of the monitoring
626 network and observed volcano-tectonic ground deformation. Natural Hazards and Earth
627 System Sciences Discussions, 3, 6117-6148.doi:10.5194/nhessd-3-6117-2015
628 Brounce, M., Kelley, K., Cottrell, E., 2014. Variations in $Fe^{3+}/\sum Fe$ of Mariana Arc Basalts and
629 Mantle Wedge fO_2. Journal of Petrology 55, 2513-2536. doi:10.1093/petrology/egu065
630 Brugger, C., Hammer, J., 2010. Crystallization Kinetics in Continuous Decompression
631 Experiments: Implications for Interpreting Natural Magma Ascent Processes. Journal of
632 Petrology 51, 1941-1965. doi:10.1093/petrology/egq044
633 Cameron, B., Walker, J., Carr, M., Patino, L., Matìas, O., Feigenson, M., 2003. Flux versus
634 decompression melting at stratovolcanoes in southeastern Guatemala. Journal of Volcanology
635 and Geothermal Research 119, 21-50. doi:10.1016/s0377-0273(02)00304-9
636 Cameron, B.I., Walker, J.A., 2006, Diverse volcanism in southeastern Guatemala: The role of
637 crustal contamination, in: eds. Rose et al., Geological Society of America Special Paper 412,
638 Volcanic Hazards in Central America, 121-139.doi:10.1130/2006.2412(07)
639 Carr, M., 1984. Symmetrical and segmented variation of physical and geochemical characteristics
640 of the central american volcanic front. Journal of Volcanology and Geothermal Research 20,

231-252. doi:10.1016/0377-0273(84)90041-6

Carr, M., Feigenson, M., Bennett, E., 1990. Incompatible element and isotopic evidence for tectonic control of source mixing and melt extraction along the Central American arc. Contributions to Mineralogy and Petrology 105, 369-380. doi:10.1007/bf00286825

Carr, M., Rose, W., Mayfield, D., 1979. Potassium content of lavas and depth to the seismic zone in central america. Journal of Volcanology and Geothermal Research 5, 387-401. doi:10.1016/0377-0273(79)90025-8

Carr, M. J., Feigenson, M. D., Patino, L. C. and Walker, J. A., 2004. Volcanism and Geochemistry in Central America: Progress and Problems, in Eiler,J. (Ed.), Inside the Subduction Factory, American Geophysical Union, Washington, D. C. doi: 10.1029/138GM09

Carr, M., Patino, L., Feigenson. M., 2007. Petrology and geochemistry of lavas, in Bundschuh, J., Alvarado, G. (Eds.), Central America: Geology, Resources, and Hazards Taylor &Francis, London, pp 565-590

Chesner, C. A., Pullinger C., and Escobar C. D., 2004. Physical and chemical evolution of San Miguel volcano, El Salvador. Geological Society of America Special Papers, 375, 213-226.doi: 10.1130/0-8137-2375-2.213

Cocker, J., Griffin, B., Muehlenbachs, K., 1982. Oxygen and carbon isotope evidence for seawater-hydrothermal alteration of the Macquarie Island ophiolite. Earth and Planetary Science Letters 61, 112-122. doi:10.1016/0012-821x(82)90043-7

Couch, S., 2003. Experimental investigation of crystallization kinetics in a haplogranite system. American Mineralogist 88, 1471-1485. doi:10.2138/am-2003-1011

Davidson, J., Tepley, F., 1997. Recharge in Volcanic Systems: Evidence from Isotope Profiles of Phenocrysts. Science 275, 826-829. doi:10.1126/science.275.5301.826

Davies, J., Stevenson, D., 1992. Physical model of source region of subduction zone volcanics. Journal of Geophysical Research 97, 2037-2070. doi:10.1029/91jb02571

Devine, J., Gardner, J., Brack, H., Layne, G., Rutherford, M., 1995. Comparison of microanalytical

667 methods for estimating H_2O contents of silicic volcanic glasses. American Mineralogist 80,
668 319-328. doi:10.2138/am-1995-3-413
669 Dohmen, R., Blundy, J., 2014. A predictive thermodynamic model for element partitioning between
670 plagioclase and melt as a function of pressure, temperature and composition. American Journal
671 of Science 314, 1319-1372. doi:10.2475/09.2014.04
672 Donnelly, T. W., D. Beets, M. J. Carr, T. Jackson, G. Klaver, J. Lewis, Maury, R., H. Schellekens,
673 A. Smith, G. Wadge & D. Westerkamp, 1990, History and tectonic setting of Caribbean
674 magmatism: In: Dengo, G. (Ed.), The Geology of North America, v. H., The Caribbean
675 Region, chapter 13, p. 339 – 374
676 Eichelberger, J., Chertkoff, D., Dreher, S., Nye, C., 2000. Magmas in collision: Rethinking
677 chemical zonation in silicic magmas. Geology 28, 603. doi:10.1130/0091-
678 7613(2000)28<603:micrcz>2.0.co;2
679 Eiler, J., Carr, M., Reagan, M., Stolper, E., 2005. Oxygen isotope constraints on the sources of
680 Central American arc lavas. Geochemistry, Geophysics, Geosystems 6.
681 doi:10.1029/2004gc000804
682 Ersoy, Y., Helvacı, C., 2010. FC–AFC–FCA and mixing modeler: A Microsoft® Excel© spreadsheet
683 program for modeling geochemical differentiation of magma by crystal fractionation, crustal
684 assimilation and mixing. Computers & Geosciences 36, 383-390.
685 doi:10.1016/j.cageo.2009.06.007
686 Escobar, C. D., 2003. San Miguel Volcano and its Volcanic Hazards, El Salvador. Unpublished
687 thesis, Michigan Tchnological University (USA).
688 Feigenson, M., Carr, M., 1986. Positively correlated Nd and Sr isotope ratios of lavas from the
689 Central American volcanic front. Geol 14, 79. doi:10.1130/0091-
690 7613(1986)14<79:pcnasi>2.0.co;2
691 Fiege, A., Vetere, F., Iezzi, G., Simon, A., Holtz, F., 2015. The roles of decompression rate and
692 volatiles (H_2O + Cl ± CO_2±S) on crystallization in (trachy-) basaltic magma. Chem. Geol., 411,

310-322.

Foden, J., Green, D., 1992. Possible role of amphibole in the origin of andesite: some experimental and natural evidence. Contr. Mineral. and Petrol. 109, 479-493. doi:10.1007/bf00306551

Ghiorso, M., Sack, R., 1995. Chemical mass transfer in magmatic processes IV. A revised and internally consistent thermodynamic model for the interpolation and extrapolation of liquid-solid equilibria in magmatic systems at elevated temperatures and pressures. Contribution to Mineralogy and Petrology 119, 197-212. doi:10.1007/bf00307281

Gonnermann H. M., Manga M., 2013. Dynamics of magma ascent in the volcanic conduit, in: Fagents, S., Gregg, T., Lopes, R. (Eds.), Modeling volcanic processes. Cambridge University Press, Cambridge.

Granieri, D., Salerno, G., Liuzzo, M., La Spina, A., Giuffrida, G., Caltabiano, T.,Giudice,G., Gutierrez, E.,Montalvo, F., Burton,M. R., Papale, P., 2015. Emission of gas and atmospheric dispersion of SO2 during the December 2013 eruption at San Miguel volcano (El Salvador, Central America). Geophysical Research Letters, 42(14), 5847-5854. doi:10.1002/2015GL064660.

Grove, T., Juster, T., 1989. Experimental investigations of low-Ca pyroxene stability and olivine-pyroxene-liquid equilibria at 1-atm in natural basaltic and andesitic liquids. Contributions to Mineralogy and Petrology, 103, 287-305. doi:10.1007/bf00402916

Hammer, J., Rutherford, M., 2002. An experimental study of the kinetics of decompression-induced crystallization in silicic melt. Journal of Geophysical Research 107. doi:10.1029/2001jb000281

Hibbard, M., 1981. The magma mixing origin of mantled feldspars. Contributions to Mineralogy and Petrology, 76, 158-170. doi:10.1007/bf00371956

Iezzi, G., Mollo, S., Shahini, E., Cavallo, A., Scarlato, P., 2014. The cooling kinetics of plagioclase feldspar as revealed by electron-microprobe mapping. American Mineralogist 99, 898-907. doi:10.2138/am.2014.4626

719 Iezzi, G., Mollo, S., Torresi, G., Ventura, G., Cavallo, A., Scarlato, P., 2011. Experimental
720 solidification of an andesitic melt by cooling. Chemical Geology 283, 261-273.
721 doi:10.1016/j.chemgeo.2011.01.024
722 Izbekov, P., Eichelberger, J., Ivanov, B., 2004. The 1996 Eruption of Karymsky Volcano,
723 Kamchatka: Historical Record of Basaltic Replenishment of an Andesite Reservoir. Journal of
724 Petrology 45, 2325-2345. doi:10.1093/petrology/egh059
725 Kirkpatrick, R., Robinson, G., Hays, J., 1976. Kinetics of crystal growth from silicate melts:
726 Anorthite and diopside. J. Geophys. Res., 81, 5715-5720. doi:10.1029/jb081i032p05715
727 Kress, V., Carmichael, I., 1991. The compressibility of silicate liquids containing Fe2O3 and the
728 effect of composition, temperature, oxygen fugacity and pressure on their redox states.
729 Contributions to Mineralogy and Petrology ,108, 82-92. doi:10.1007/bf00307328
730 Lanzafame, G., Mollo, S., Iezzi, G., Ferlito, C., Ventura, G., 2013. Unraveling the solidification
731 path of a pahoehoe "cicirara" lava from Mount Etna volcano. Bull. Volcanol. 75, 703.
732 doi:http://dx.doi.org/10.1007/s00445-013-0703-8.
733 Le Bas, M., Maitre, R., Streckeisen, A., Zanettin, B., 1986. A Chemical Classification of Volcanic
734 Rocks Based on the Total Alkali-Silica Diagram. Journal of Petrology 27, 745-750.
735 doi:10.1093/petrology/27.3.745
736 Le Maitre, R., 2002. Igneous rocks. Cambridge University Press, Cambridge, U.K.
737 Leeman, W., Carr, M., Morris, J., 1994. Boron geochemistry of the Central American Volcanic Arc:
738 Constraints on the genesis of subduction-related magmas. Geochimica et Cosmochimica Acta
739 58, 149-168. doi:10.1016/0016-7037(94)90453-7
740 MacMillan, I., Gans, P., Alvarado, G., 2004. Middle Miocene to present plate tectonic history of the
741 southern Central American Volcanic Arc. Tectonophysics 392, 325-348.
742 doi:10.1016/j.tecto.2004.04.014
743 Martinez-Hackert, B., Bajo, J., Escobar, D., Gutierrez, E., Mixco, L., Hernandez, W., 2015,
744 Chaparrastique (San Mighel) Volcano Eruptions since Dec. 29th, 2013, El Salvador, Abstract

V23A-3087, presented at 2015 Fall Meeting, AGU, San Francisco, Calif., 14-18 Dec.

Mattey, D., Lowry, D., Macpherson, C., 1994. Oxygen isotope composition of mantle peridotite. Earth and Planetary Science Letters 128, 231-241. doi:10.1016/0012-821x(94)90147-3

Mollo, S., Giacomoni, P., Andronico, D., Scarlato, P., 2015. Clinopyroxene and titanomagnetite cation redistributions at Mt. Etna volcano (Sicily, Italy): Footprints of the final solidification history of lava fountains and lava flows. Chemical Geology, 406, 45-54. doi:10.1016/j.chemgeo.2015.04.017

Mollo, S., Misiti, V., Scarlato, P., Soligo, M., 2012a. The role of cooling rate in the origin of high temperature phases at the chilled margin of magmatic intrusions. Chemical Geology, 322-323, 28-46. doi:10.1016/j.chemgeo.2012.05.029

Mollo, S., Iezzi, G., Ventura, G., Cavallo, A., Scarlato, P., 2012b. Heterogeneous nucleation mechanisms and formation of metastable phase assemblages induced by different crystalline seeds in a rapidly cooled andesitic melt. Journal of Non-Crystalline Solids 358, 1624-1628. doi:10.1016/j.jnoncrysol.2012.04.010

Mollo, S., Putirka, K., Iezzi, G., Del Gaudio, P., Scarlato, P., 2011. Plagioclase-melt (dis)equilibrium due to cooling dynamics: Implications for thermometry, barometry and hygrometry. Lithos 125, 221-235. doi:10.1016/j.lithos.2011.02.008

Morimoto, N., 1988. Nomenclature of Pyroxenes. Mineralogy and Petrology 39, 55-76. doi:10.1007/bf01226262

Muncill, G.E., Lasaga, A.C., 1987. Crystal-growth kinetics of plagioclase in igneous systems: One-atmosphere experiments and application of a simplified growth model. American Mineralogist 72, 299-311

Namur, O., Charlier, B., Toplis, M., Vander Auwera, J., 2011. Prediction of plagioclase-melt equilibria in anhydrous silicate melts at 1-atm. Contributions to Mineralogy and Petrology 163, 133-150. doi:10.1007/s00410-011-0662-z

Neill, O., Larsen, J., Izbekov, P., Nye, C., 2015. Pre-eruptive magma mixing and crystal transfer

771 revealed by phenocryst and microlite compositions in basaltic andesite from the 2008 eruption
772 of Kasatochi Island volcano. American Mineralogist 100, 722-737. doi:10.2138/am-2015-4967
773 Patino, L., Carr, M., Feigenson, M., 2000. Local and regional variations in Central American arc
774 lavas controlled by variations in subducted sediment input. Contributions to Mineralogy and
775 Petrology 138, 265-283. doi:10.1007/s004100050562
776 Plank, T., Langmuir, C., 1998. The chemical composition of subducting sediment and its
777 consequences for the crust and mantle. Chemical Geology 145, 325-394. doi:10.1016/s0009-
778 2541(97)00150-2
779 Protti, M., McNally, K., Pacheco, J., González, V., Montero, C., Segura, J., Brenes, J.,Barboza, V.,
780 Malavassi, E., Güendel, F., Simila, G., Rojas, D., Velasco, A., Mata, A., Schillinger, W., 1995.
781 The March 25, 1990 (M w = 7.0, M L = 6.8), earthquake at the entrance of the Nicoya Gulf,
782 Costa Rica: Its prior activity, foreshocks, aftershocks, and triggered seismicity. J. Geophys.
783 Res. 100, 20345. doi:10.1029/94jb03099
784 Pupier, E., Duchene, S., Toplis, M., 2007. Experimental quantification of plagioclase crystal size
785 distribution during cooling of a basaltic liquid. Contributions to Mineralogy and Petrology 155,
786 555-570. doi:10.1007/s00410-007-0258-9
787 Putirka, K., 2005a. Mantle potential temperatures at Hawaii, Iceland, and the mid-ocean ridge
788 system, as inferred from olivine phenocrysts: Evidence for thermally driven mantle plumes.
789 Geochemistry, Geophysics, Geosystems 6, n/a-n/a. doi:10.1029/2005gc000915
790 Putirka, K., 2005b. Igneous thermometers and barometers based on plagioclase + liquid equilibria:
791 Tests of some existing models and new calibrations. American Mineralogist 90, 336-346.
792 doi:10.2138/am.2005.1449
793 Putirka, K., 2008. Thermometers and barometers for volcanic systems. In: Putirka, K.D., Tepley, F.
794 (Eds.), Minerals, Inclusions and Volcanic Processes. Reviews in mineralogy and geochemistry
795 69, pp. 61–120.
796 Richer, M., Mann, C., Stix, J., 2004. Mafic magma injection triggers eruption at Ilopango Caldera,

797 El Salvador, Central America. In: W.J. Rose, J.J. Bommer, D.L. López, M.J. Carr and
798 J.J.Major (eds.): Natural hazards in El Salvador. Geological Society of America, Special Paper
799 375, Boulder CO, 2004, pp.175–189.doi:10.1130/0-8137-2375-2.175
800 Roeder, P., Emslie, R., 1970. Olivine-liquid equilibrium. Contributions to Mineralogy and
801 Petrology 29, 275-289. doi:10.1007/bf00371276
802 Roggensack, K., 2001. Unraveling the 1974 eruption of Fuego volcano (Guatemala) with small
803 crystals and their young melt inclusions. Geology 29, 911. doi:10.1130/0091-
804 7613(2001)029<0911:uteofv>2.0.co;2
805 Roggensack, K., Hervig, R., McKnight, S., Williams, S., 1997. Explosive Basaltic Volcanism from
806 Cerro Negro Volcano: Influence of Volatiles on Eruptive Style. Science 277, 1639-1642.
807 doi:10.1126/science.277.5332.1639
808 Rutherford, M., 2008. Magma Ascent Rates. Reviews in Mineralogy and Geochemistry 69, 241-271.
809 doi:10.2138/rmg.2008.69.7
810 Sadofsky, S., Portnyagin, M., Hoernle, K., van den Bogaard, P., 2007. Subduction cycling of
811 volatiles and trace elements through the Central American volcanic arc: evidence from melt
812 inclusions. Contributions to Mineralogy and Petrology 155, 433-456. doi:10.1007/s00410-007-
813 0251-3
814 Sato, H., 1995. Textural difference between pahoehoe and aa lavas of Izu-Oshima volcano, Japan -
815 an experimental study on population density of plagioclase. Journal of Volcanology and
816 Geothermal Research 66, 101-113. doi:10.1016/0377-0273(94)00055-l
817 Scarlato, P., Kattan, C., Papale, P., Gresta, S., 2014, International cooperation during volcanic
818 crisis: an example from the Italy-El Salvador monitoring system installed at Chaparrastique
819 volcano, El Salvador. Cities on Volcanoes 8.
820 Schiavi, F., Walte, N., Keppler, H., 2009. First in situ observation of crystallization processes in a
821 basaltic-andesitic melt with the moissanite cell. Geology 37, 963-966. doi:10.1130/g30087a.1
822 Shcherbakov, V., Plechov, P., Izbekov, P., Shipman, J., 2010. Plagioclase zoning as an indicator of

magma processes at Bezymianny Volcano, Kamchatka. Contributions to Mineralogy and Petrology 162, 83-99. doi:10.1007/s00410-010-0584-1

Sisson, T., Layne, G., 1993. H2O in basalt and basaltic andesite glass inclusions from four subduction-related volcanoes. Earth and Planetary Science Letters 117, 619-635. doi:10.1016/0012-821x(93)90107-k

Smith, R., Lofgren, G., 1983. An analytical and experimental study of zoning in plagioclase. Lithos 16, 153-168. doi:10.1016/0024-4937(83)90012-9

Smith, V., Tiller, W., Rutter, J., 1955. A mathematical analysis of solute redistribution during solidification. Can. J. Phys. 33, 723-745. doi:10.1139/p55-089

Sparks, S., Sigurdsson, H., Wilson, L., 1977. Magma mixing: a mechanism for triggering acid explosive eruptions. Nature 267, 315-318. doi:10.1038/267315a0

Staudigel, H., Davies, G., Hart, S., Marchant, K., Smith, B., 1995. Large scale isotopic Sr, Nd and O isotopic anatomy of altered oceanic crust: DSDP/ODP sites417/418. Earth and Planetary Science Letters 130, 169-185. doi:10.1016/0012-821x(94)00263-x

Streck, M., Dungan, M., Malavassi, E., Reagan, M., Bussy, F., 2002. The role of basalt replenishment in the generation of basaltic andesites of the ongoing activity at Arenal volcano, Costa Rica: evidence from clinopyroxene and spinel. Bulletin of Volcanology 64, 316-327. doi:10.1007/s00445-002-0209-2

Sun, S., McDonough, W., 1989. Chemical and isotopic systematics of oceanic basalts: implications for mantle composition and processes. Geological Society, London, Special Publications 42, 313-345. doi:10.1144/gsl.sp.1989.042.01.19

Syracuse, E., Abers, G., 2006. Global compilation of variations in slab depth beneath arc volcanoes and implications. Geochemistry, Geophysics, Geosystems 7, n/a-n/a. doi:10.1029/2005gc001045

Teng, H.H., 2013. How ions and molecules organize to form crystals. Elements, 9, 189–194

Tepley, F., Davidson, J., Tilling, R., ARTH, J., 2000. Magma Mixing, Recharge and Eruption

849 Histories Recorded in Plagioclase Phenocrysts from El Chichon Volcano, Mexico. Journal of
850 Petrology 41, 1397-1411. doi:10.1093/petrology/41.9.1397
851 Tonarini, S., Agostini, S., Doglioni, C., Innocenti, F., Manetti, P., 2007. Evidence for serpentinite
852 fluid in convergent margin systems: The example of El Salvador (Central America) arc lavas.
853 Geochemistry, Geophysics, Geosystems 8, 9. doi:10.1029/2006gc001508
854 Toramaru, A., Noguchi, S., Oyoshihara, S., Tsune, A., 2008. MND(microlite number density) water
855 exsolution rate meter. Journal of Volcanology and Geothermal Research 175, 156-167.
856 doi:10.1016/j.jvolgeores.2008.03.035
857 Tsuchiyama, A., 1985. Dissolution kinetics of plagioclase in the melt of the system diopside-albite-
858 anorthite, and origin of dusty plagioclase in andesites. Contributions to Mineralogy and
859 Petrology 89, 1-16. doi:10.1007/bf01177585
860 Tsuchiyama, A., Takahashi, E., 1983. Melting kinetics of a plagioclase feldspar. Contr. Mineral.
861 andPetrol. 84, 345-354. doi:10.1007/bf01160286
862 Vetere, F., Iezzi, G., Behrens, H., Holtz, F., Ventura, G., Misiti, V., Cavallo, A., Mollo, S., Dietrich,
863 M., 2015. Glass forming ability and crystallization behaviour of sub-alkaline silicate melts.
864 Earth-Science Reviews 150, 25-44. doi:10.1016/j.earscirev.2015.07.001
865 vonQuadt, A., 1997. U–Pb zircon and Sr–Nd–Pb whole-rock investigations from the continental
866 deep drilling (KTB). Geologische Rundschau 86, S258-S271. doi:10.1007/pl00014659
867 Wade, J., Plank, T., Melson, W., Soto, G., Hauri, E., 2006. The volatile content of magmas from
868 Arenal volcano, Costa Rica. Journal of Volcanology and Geothermal Research 157, 94-120.
869 doi:10.1016/j.jvolgeores.2006.03.045
870 Walker, R. J., Morgan, J. W., & Horan, M. F., 1995. Osmium-187 enrichment in some plumes:
871 evidence for core-mantle interaction?. Science, 269(5225), 819-822. doi:
872 10.1126/science.269.5225.819
873 Zhang, Y., Ni, H., Chen, Y., 2010. Diffusion Data in SilicateMelts. Reviews in Mineralogy and
874 Geochemistry 72, 311-408. doi:10.2138/rmg.2010.72.8

Figure captions

Fig.1. Schematic map showing the Central American volcanic arc (CAVA), where volcanism occurs above the plate boundary between the subducting Cocos plate and the overriding Caribbean plate (a). The ash plume of the Chaparrastique vulcanian-type eruption captured by the Suomi NPP satellite (b). Seismic monitoring stations of VSMG, RANC, and LACA located, respectively, at 1 km north, 2 km east, and 3 km south-east to the volcanic crater where twelve rock samples were collected (c).

Fig.2. Textural and compositional characteristics of the scoria clasts. Larger Fo-rich poikilitic olivines include sub-rounded Mg-rich, Usp-rich titanomagnetites (a). Smaller Fo-poor olivines are accompanied by the Mg-poor, Usp-poor titanomagnetites with incomplete textures and glass embayments resulting from the agglomeration of bleb-like grains (b). Orthopyroxenes are less frequently observed and sometimes occur as larger crystals partly enclosing smaller clinopyroxenes (c). Plagioclases are characterized by dark-grey, partly corroded An_{53-65} cores, light-grey, coarsely sieve-textured An_{80-84} mantles, and grey, euhedral to sub-euhedral An_{77-80} rims (d, e, f). Plagioclase rims results from the attachment of a number of groundmass microlites growing as tabular crystals (g, h, i). Ol, olivine. Timt, titanomagnetite. Opx, orthopyroxene. Cpx, clinopyroxene. Pl, plagioclase. Fo, forsterite. Usp, ulvospinel. En, enstatite. Di, diopside. An, anorthite.

Fig.3. TAS (total alkali vs. silica; Le Bas et al., 1986) diagram showing calc-alkaline basalts (CH1-CH2) and moderately (CH3-CH6) to more differentiated (CH7-CH12) basaltic andesites (a). According to the SiO_2 vs. K_2O diagram (LeMaitre, 2002), the Chaparrastique volcanic products have medium-K affinity (b). The chondrite-normalized pattern (Sun and McDonough, 1989) of REE (rare earth elements) exhibits sub-parallel trends shifting towards progressive REE enrichments from CH1 to CH12 (c). The primordial mantle-normalized pattern (Sun and

McDonough, 1989) of trace elements shows typical features of arc magmas, with LILE (large ion lithophile elements) to HFSE (high field strength elements) ratios higher than the primitive mantle values (d).

Fig.4. Predictions for the crystallization temperatures of olivine phenocrysts using the thermometer of Putirka (2005a) and assuming equilibrium with the bulk rock compositions through the Fe-Mg exchange of Roeder and Emslie (1970) (a). Test for equilibrium using the plagioclase-based model of Namur et al. (2012). Temperature estimates for plagioclase are obtained by the thermometer of Putirka (2005b) (b). According to Putirka (2008), the Fe-Mg exchange between clinopyroxene and orthopyroxene suggests equilibrium crystallization conditions. The two-pyroxenes equilibrated at relative low temperatures (c) and low pressures (d).

Fig.5. Phase equilibrium experiments of Foden and Green (1992) conducted at P = 200 MPa and reproducing the crystallization sequence of olivine, olivine + plagioclase, and olivine + plagioclase + pyroxene that is observed in the natural products. The experimental temperatures of Foden and Green (1992) closely agrees with the saturation temperatures predicted by olivine-, plagioclase-, and pyroxene-based thermometers, evidencing primary nucleation and growth of olivine and plagioclase, and subordinated formation of pyroxene. The lack of amphibole in the eruptive products is in accordance with low-P crystallization conditions in which the amphibole saturation surface is encountered only at T < 950 °C.

Fig.6. Comparison between major oxides of bulk rocks from this study and MELTS (Ghiorso and Sack, 1995) simulations conducted using as starting liquid the most primitive CH1 basalt, and initiated from the superliquidus temperature of 1170 °C and continued along a fractional crystallization path (Table 3s submitted as supplementary material). Dotted lines indicate the appearance of the mineral phase as suggested by MELTS thermodynamics. Ol, olivine. Pl,

927 plagioclase. Cpx, clinopyroxene. Opx, orthopyroxene. Sp, spinel (a). Mixing and fractional
928 crystallization processes modelled by the Excel spreadsheet of Ersoy and Helvaci (2010). The
929 original partition coefficients set in the spreadsheet were used to derive the fractional crystallization
930 vectors of REE (c), HFSE (b), and TE (d). While these vectors describe an implausible magmatic
931 evolution for the Chaparrastique products, mixing (straight) lines joining CH1 and CH12 end-
932 members successfully model the bulk rock variability.
933
934 Fig.7. Chemical profiles carried out far enough away from the plagioclase surface (see also Table
935 4s) reveal showing chemical gradients at the crystal-melt interface causing enrichments of cations
936 incompatible with plagioclase crystal lattice (a). The lattice strain equation of Dohmen & Blundy
937 (2014) predicts that, upon the effect of equilibrium crystallization, $\ln K_{Mg}$ increases linearly with
938 1/T. The partitioning of Mg measured between plagioclase sodic core (or calcic mantle) and CaO-
939 poor (or CaO-rich) bulk rocks yields values that closely resemble those predicted by the
940 thermodynamic equation. In contrast, partition coefficients measured as the ratio between
941 plagioclase rim and matrix glass show values much higher than those expected for equilibrium
942 crystallization, as for the case K_{Mg}^{app} (i.e., disequilibrium growth) > K_{Mg}^{true} (i.e., equilibrium growth)
943 (b). Assuming that the advancing plagioclase rim does not violate the condition of crystallization
944 into an infinite melt reservoir, the value of K_{Mg}^{app} can be modelled as a function of melt and crystal
945 parameters and can be ascribed to rapid plagioclase growth velocities of ~2-7 × 10^{-8} cm/s (c).
946
947 Fig.8. U/La vs. Ba/Th diagram based on soluble/insoluble element pairs. Using these element ratios,
948 Cameron et al. (2002) modelled the role played by melts and fluids (grey trajectories) derived from
949 the subducted slab for the partial melting of the mantle wedge (a). La/Sm vs. Ba/La diagram based
950 on ratios of elements that are not highly fluid mobile in arc systems, such as the REE and HFSE.
951 This diagram allows to evidence the contribution of to the mantle wedge of melt-like components

952 derived from the subducted slab (b). $^{87}Sr/^{86}Sr$ vs. $\delta^{18}O$ diagram that serve to discriminate crustal and
953 source contamination. Cameron and Walker (2006) modelled the mixing trajectories between the
954 sediment-modified mantle (blue trajectory) and crustal contaminants (green trajectory) (c). $^{87}Sr/^{86}Sr$
955 vs. $^{143}Nd/^{144}Nd$ diagram shows evidence of crustal contamination for rocks in Guatemala that are
956 behind the volcanic front. However, most of the volcanic products in Central America define an
957 array with positive slop that represents a mix between the enriched MORB source and the
958 subducted slab (d). EM, enriched MORB source. OC, oceanic crust. CS, carbonate sediments. HS,
959 hemipelagic sediments. DM, depleted MORB source.

Figure1

Click here to download high resolution image

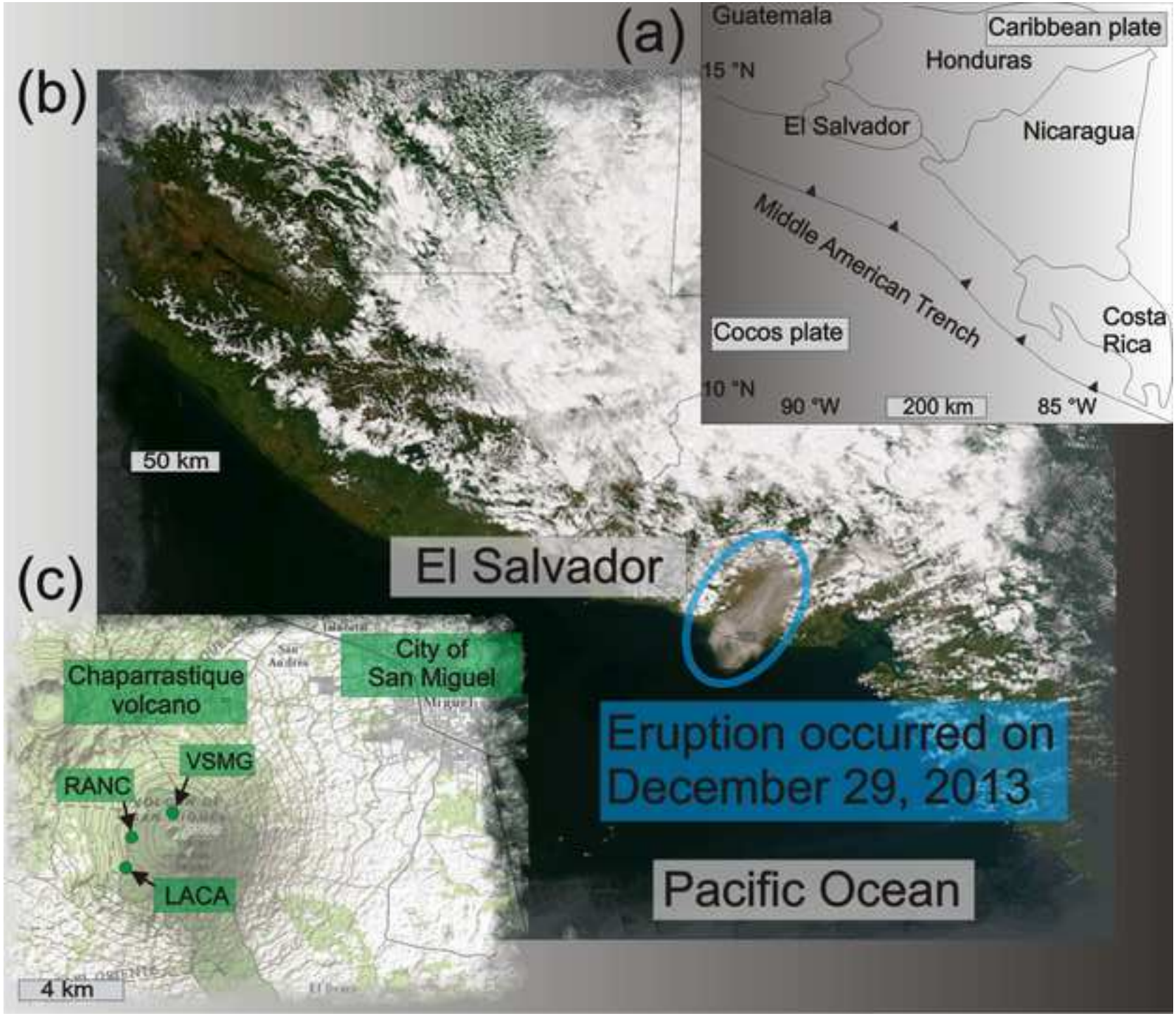

Figure2
Click here to download high resolution image

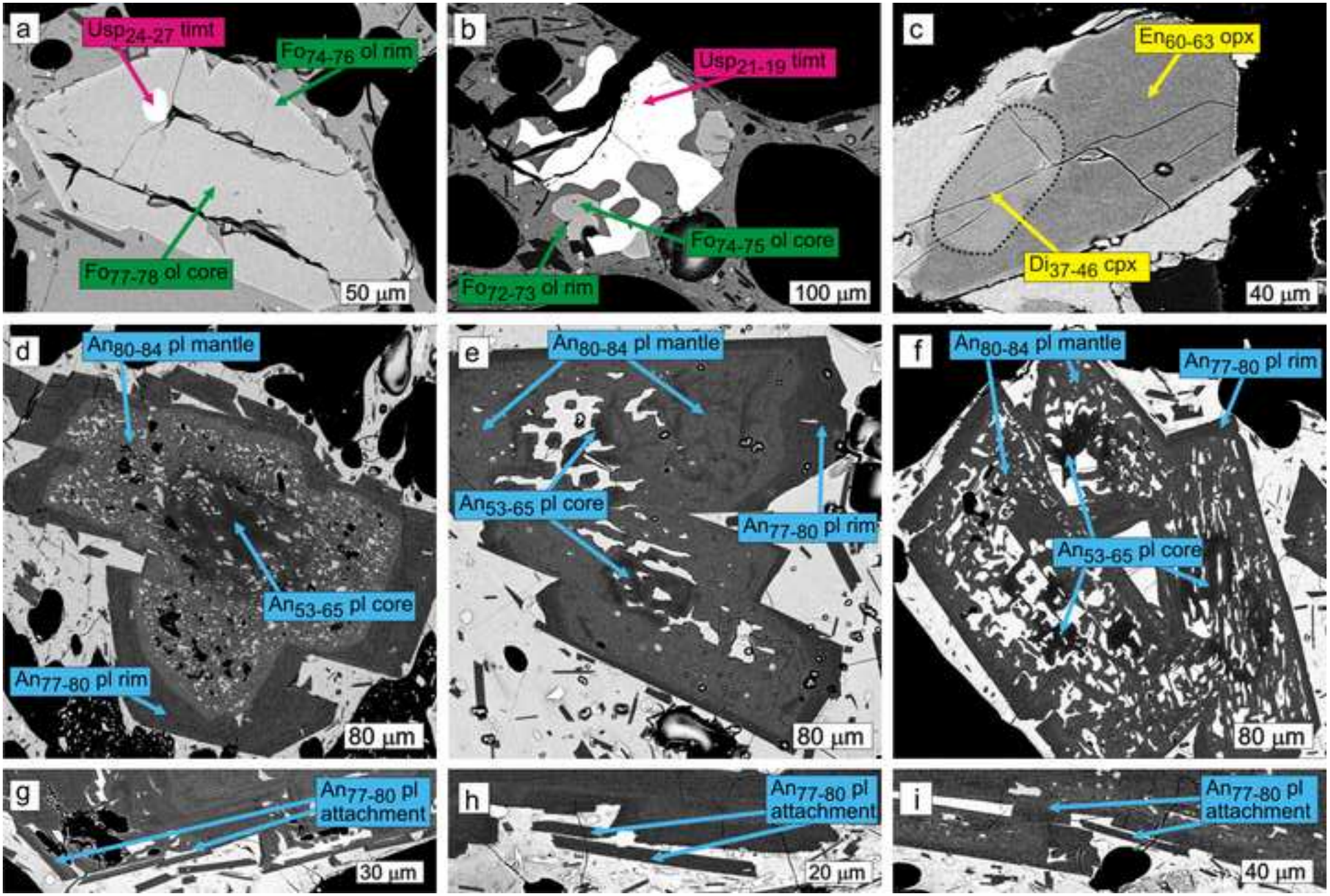

Figure3

Click here to download high resolution image

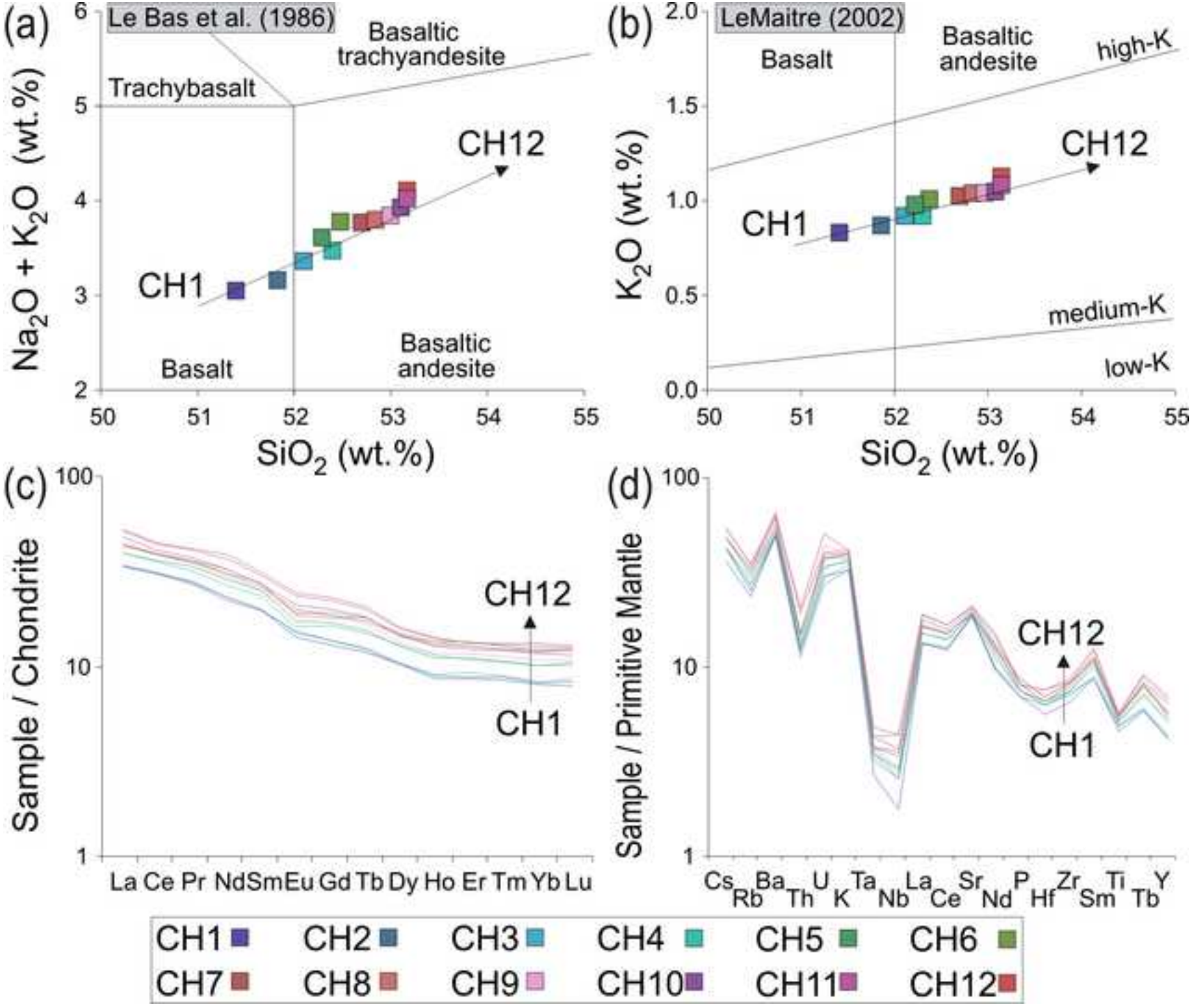

Figure4
Click here to download high resolution image

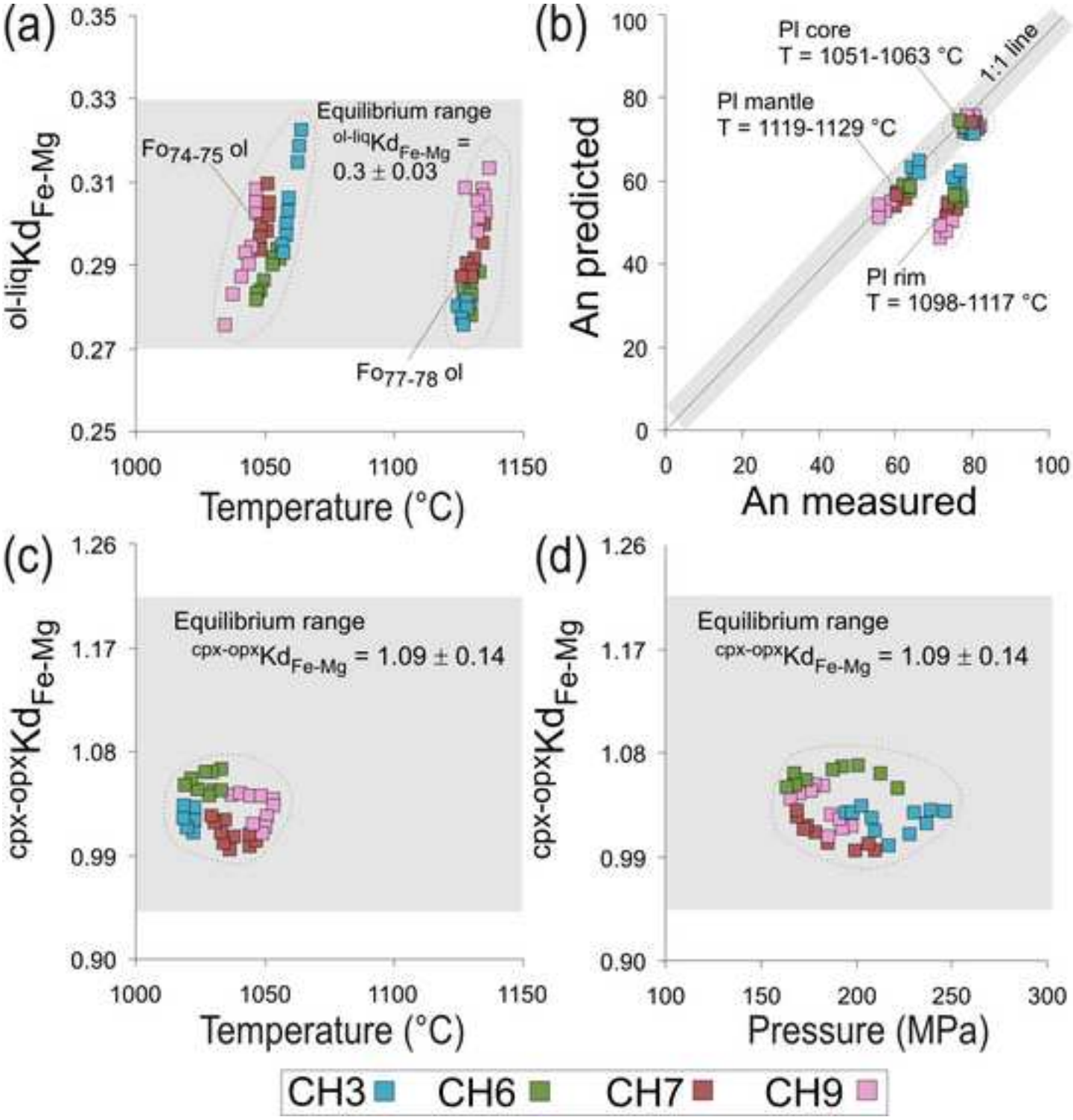

Figure5

Click here to download high resolution image

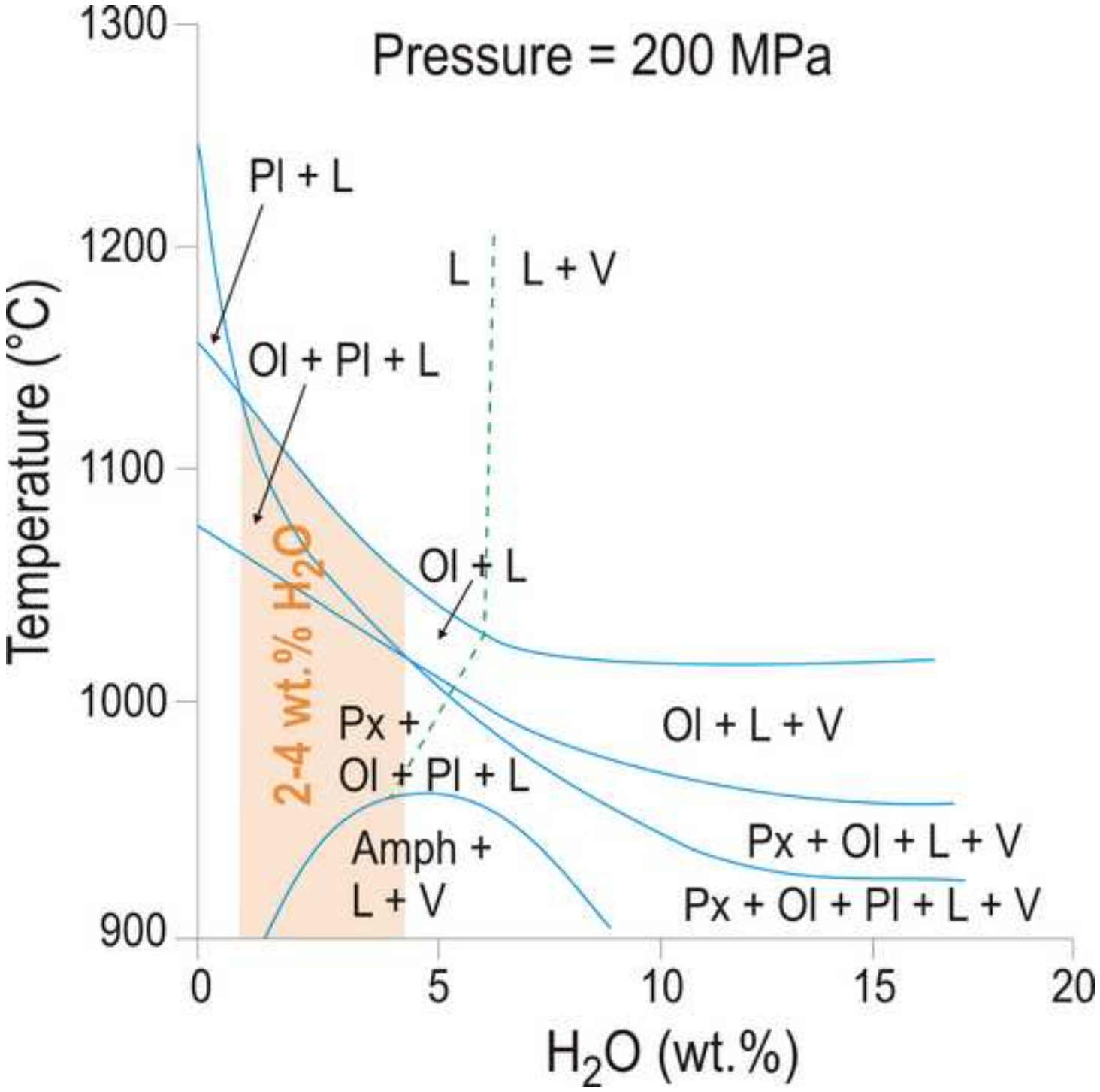

Figure6

Click here to download high resolution image

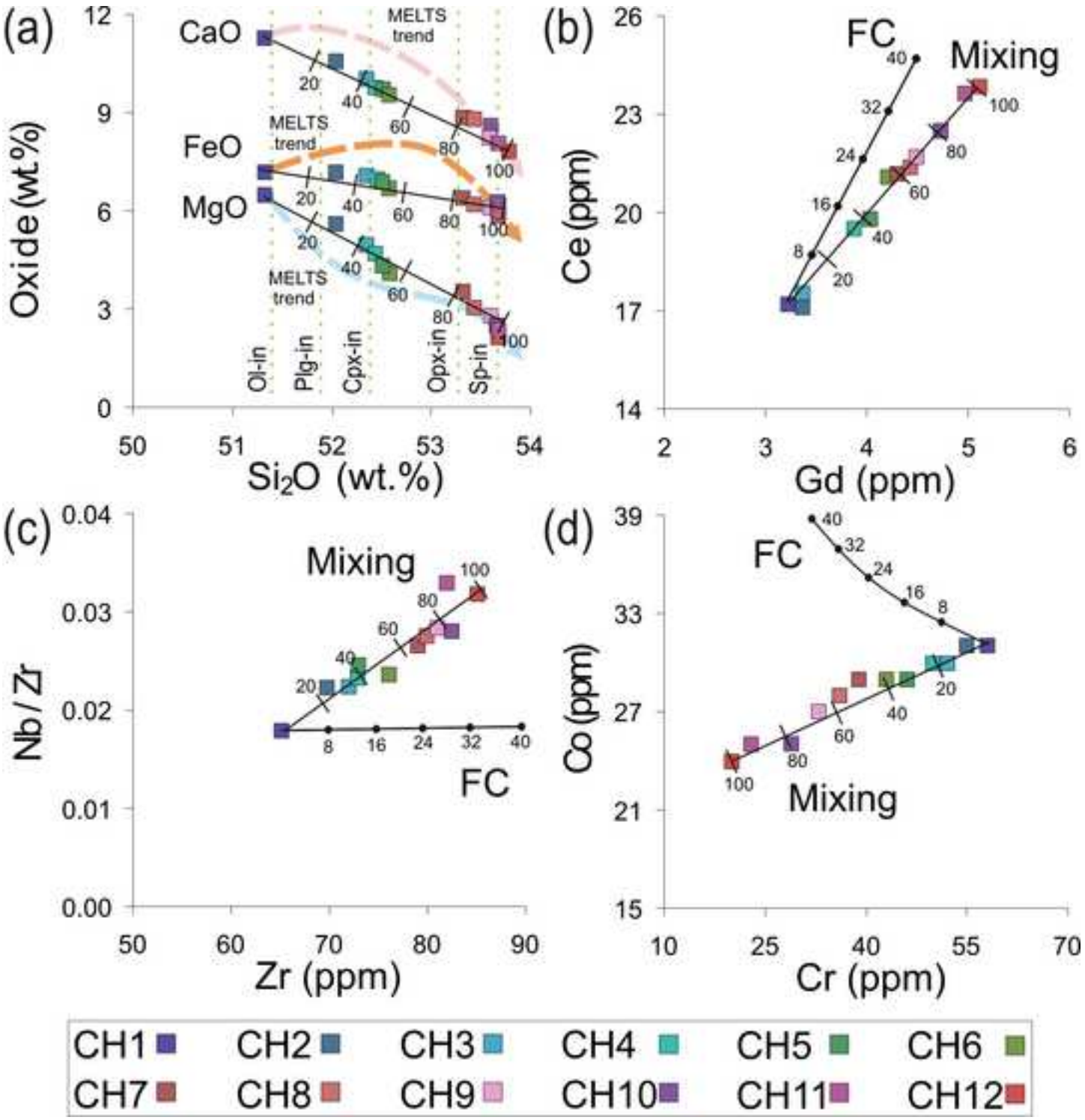

Figure7

Click here to download high resolution image

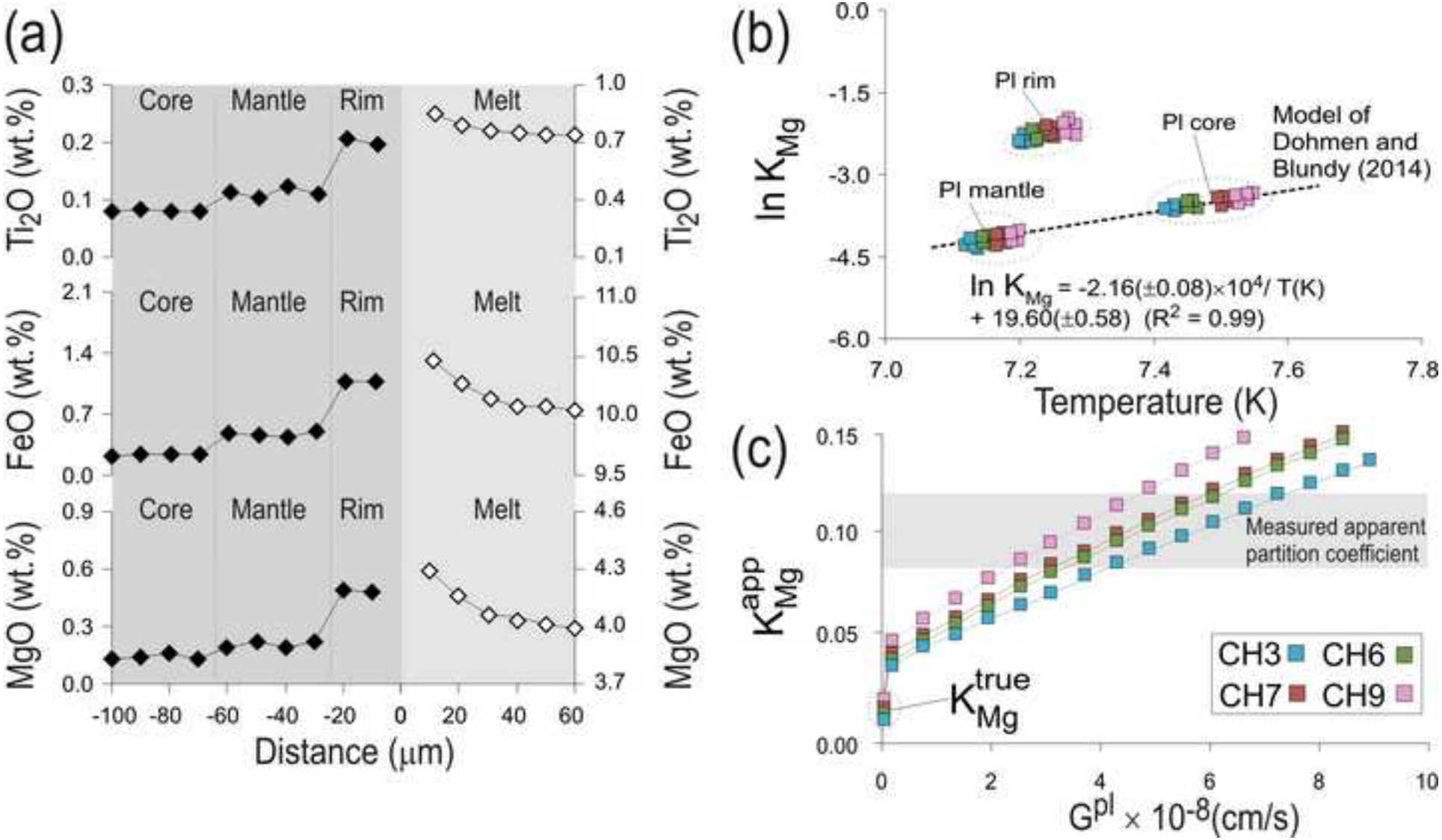

Figure8

Click here to download high resolution image

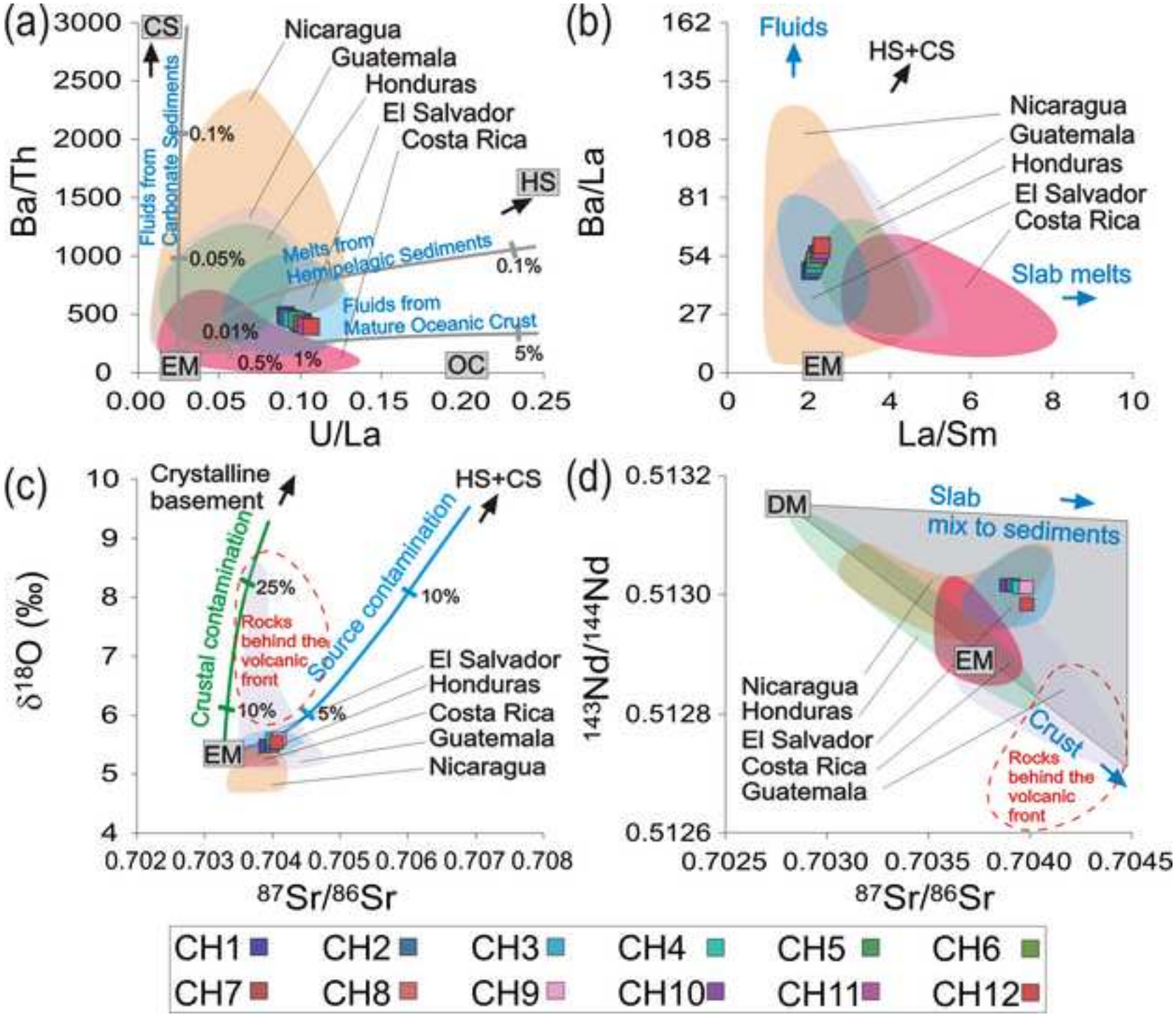

Table1S

Click here to download Background dataset for online publication only: Table1S.xls

Table2S

Click here to download Background dataset for online publication only: Table2S.xls

Table3S

Click here to download Background dataset for online publication only: Table3S.xls

Table4S

Click here to download Background dataset for online publication only: Table4S.xls

Table5S

Click here to download Background dataset for online publication only: Table5S.xls